

**Investigation of  
the  $a_0^+$  (980)-Resonance  
in the Reaction  $pp \rightarrow dK^+ \overline{K}^0$   
at an Excess Energy  
of  $Q=46$  MeV  
with ANKE**

Inaugural-Dissertation  
zur  
Erlangung des Doktorgrades  
der Mathematisch-Naturwissenschaftlichen Fakultät  
der Universität zu Köln

vorgelegt von  
Vera Kleber  
aus Karlsruhe

Köln, 2003

Berichterstatter:

Prof. Dr. H. Ströher  
Prof. Dr. H. Paetz gen. Schieck

Tag der Prüfung:

17. Februar 2003

## Zusammenfassung

Ein wesentliches Ziel des Experimentierprogramms am Spektrometer ANKE, das sich an einem internen Targetplatz des COoler SYnchrotrons COSY-Jülich befindet, ist die Untersuchung der leichten skalaren Resonanzen  $a_0(980)/f_0(980)$  nahe der  $K\bar{K}$  Produktionsschwelle. Vorgesehen ist die Messung der  $a_0/f_0$ -Produktion in Hadron-induzierten Reaktionen mit verschiedenen Isospin-Einstellungen im Eingangskanal, d.h. in  $pp$ -,  $pn$ -,  $pd$ - und  $dd$ -Reaktionen. Die ersten beiden Experimente wurden Anfang 2001 und 2002 für den  $pp$ -Kanal bei Strahlenergien von  $T_p = 2.65$  GeV ( $Q = 46$  MeV oberhalb der  $K\bar{K}$ -Schwelle) und 2.83 GeV ( $Q = 103$  MeV) durchgeführt. Beide Messungen zielten ab auf den Nachweis koinzidenter  $dK^+$  bzw.  $d\pi^+$  Ereignisse, um die  $a_0^+(980)$  Resonanz in den Reaktionsketten  $pp \rightarrow da_0^+ \rightarrow dK^+\bar{K}^0/d\pi^+\eta$  über eine „Missing Mass“-Analyse zu untersuchen.

Im Rahmen dieser Doktorarbeit wurden beide Messungen mit Hilfe von Monte-Carlo Simulationen vorbereitet und die Durchführung der zwei bzw. drei Wochen dauernden Strahlzeiten organisiert und begleitet. Im Anschluss an die Messungen wurden die Daten analysiert, wobei der Schwerpunkt bei koinzidenten  $dK^+$ -Ereignissen aus der ersten Messung lag.

Mithilfe der ANKE-Reichweitenteleskope, die auf die Identifikation von  $K^+$ -Mesonen bei hohem Untergrund optimiert sind, konnten Kaonen über ihre Flugzeit und ihren Energieverlust selektiert werden. Koinzidente Deuteronen wurden über ihre Flugzeit relativ zu den  $K^+$ -Mesonen identifiziert. Eine anschließende „Missing Mass“-Analyse der  $dK^+$ -Paare zeigt ein klares Signal bei der Masse des  $\bar{K}^0$ -Mesons mit etwa 1000 Ereignissen. Für diese  $dK^+\bar{K}^0$ -Ereignisse wurde sowohl ein totaler Produktionsquerschnitt von  $\sigma_{\text{tot}} = (38 \pm 2_{\text{stat}} \pm 14_{\text{sys}})$  nb abgeleitet, als auch differentielle Massen- und Winkelverteilungen bestimmt. Der totale Wirkungsquerschnitt, der auf einer effektiven Messzeit von ca. 5 Tagen beruht, belegt, dass systematische Untersuchungen zu den skalaren Resonanzen  $a_0(980)/f_0(980)$  an ANKE möglich sind. Die Massen- und Winkelverteilungen legen einerseits nahe, dass ein signifikanter Anteil der  $K^+\bar{K}^0$ -Paare über die  $a_0^+(980)$ -Resonanz erzeugt wird, und lassen andererseits vermuten, dass auch die Endzustands-Wechselwirkung zwischen dem Deuteron und dem  $\bar{K}^0$  bei der Interpretation der Daten berücksichtigt werden muss.



## Abstract

A major goal of the experimental program at the spectrometer ANKE, which is located at an internal target position of the COoler SYnchrotron COSY–Jülich, is the investigation of the light scalar resonances  $a_0(980)/f_0(980)$  close to the  $K\bar{K}$  production threshold. It is foreseen to measure the  $a_0/f_0$  production in hadron–induced reactions with different isospin configurations in the entrance channel, i.e. in  $pp$ ,  $pn$ ,  $pd$  and  $dd$  reactions. The first two experiments were carried out in the beginning of 2001 and 2002 for the  $pp$  channel at beam energies of  $T_p = 2.65$  GeV ( $Q = 46$  MeV above the  $K\bar{K}$  threshold) and 2.83 GeV ( $Q = 103$  MeV). Both measurements aimed at the detection of coincident  $dK^+$  and  $d\pi^+$  pairs in order to investigate the  $a_0^+(980)$  resonance in the reaction chains  $pp \rightarrow da_0^+ \rightarrow dK^+\bar{K}^0/d\pi^+\eta$  with a missing–mass analysis.

In the framework of this thesis both measurements were prepared with the help of Monte–Carlo simulations and the beam times of two and three weeks were organized and conducted. After the measurements the data were analyzed, focusing on the  $dK^+$  events obtained at  $T_p = 2.65$  GeV.

With the help of the ANKE range telescopes, which are optimized for the identification of  $K^+$  mesons in a huge background of other particles, the kaons can be selected via their time–of–flight and energy losses. Coincident deuterons are identified via their time relative to the  $K^+$  mesons. A subsequent missing–mass analysis of the  $dK^+$  pairs reveals a clear peak at the mass of the  $\bar{K}^0$  meson with about 1000 events. For these  $dK^+\bar{K}^0$  events the total production cross section of  $\sigma_{\text{tot}} = (38 \pm 2_{\text{stat}} \pm 14_{\text{sys}})$  nb as well as differential mass and angular distributions have been determined. The total cross section, which is based on an effective measuring time of about 5 days, shows that systematic studies of the scalar resonances  $a_0(980)/f_0(980)$  are possible with ANKE. The mass and angular distributions indicate that a significant fraction of the  $K^+\bar{K}^0$  pairs are produced via the  $a_0^+(980)$  resonance. They also suggest that the final–state interaction between the deuteron and the  $\bar{K}^0$  has to be taken into account for the interpretation of the data.



# Contents

<b>1</b>	<b>Light Scalar Resonances</b>	<b>1</b>
1.1	Baryons and Mesons . . . . .	2
1.2	Experiments on the $a_0(980)$ Resonance . . . . .	5
1.3	$pp \rightarrow da_0^+ \rightarrow dK^+\overline{K}^0$ near Threshold . . . . .	6
<b>2</b>	<b>ANKE-Experiment on <math>a_0^+(980)</math> production</b>	<b>11</b>
2.1	The ANKE Spectrometer at COSY-Jülich . . . . .	11
2.2	Experimental Setup . . . . .	14
2.2.1	COSY Beam, Target and Magnetic Field . . . . .	14
2.2.2	The Side Detection System (SDS) . . . . .	15
2.2.3	The Forward Detection System (FDS) . . . . .	16
2.2.4	Hardware Trigger and Data Acquisition . . . . .	17
<b>3</b>	<b>Identification of <math>K^+</math> Mesons</b>	<b>19</b>
3.1	Time-of-Flight and Energy-Loss Information . . . . .	19
3.2	Background Suppression by Tracking . . . . .	21
3.3	Adjustment of the $K^+$ -Selection . . . . .	22
3.4	Data Preselection . . . . .	22
3.5	$K^+$ Momentum Reconstruction . . . . .	24
<b>4</b>	<b>Identification of Deuterons</b>	<b>27</b>
4.1	Momentum Reconstruction in the FDS . . . . .	27
4.2	Timing Information . . . . .	28
4.3	Identification of Protons and Deuterons . . . . .	29
<b>5</b>	<b>Identification of the Reaction <math>pp \rightarrow dK^+\overline{K}^0</math></b>	<b>33</b>
5.1	Identification of 3-Body-Reactions . . . . .	33
5.2	Efficiency Determination . . . . .	35
5.2.1	Cut on Energy Loss in the $\Delta E$ counters . . . . .	35
5.2.2	Side Chambers . . . . .	35
5.2.3	Forward Chambers . . . . .	36
5.3	Effectiveness of the Selection Criteria . . . . .	37

---

5.4	Analysis of $dK^+\overline{K}^0$ Events . . . . .	38
<b>6</b>	<b>Simulations on the Reaction <math>pp \rightarrow dK^+\overline{K}^0</math></b>	<b>41</b>
6.1	Total Acceptance . . . . .	41
6.2	Differential Acceptance Correction . . . . .	42
<b>7</b>	<b>Results and Interpretation</b>	<b>49</b>
7.1	Total Production Cross Section . . . . .	49
7.2	Mass Distributions . . . . .	51
7.3	Angular Distributions . . . . .	52
7.4	Conclusions . . . . .	54
<b>8</b>	<b>Outlook</b>	<b>55</b>
<b>A</b>	<b>Appendix</b>	<b>57</b>
A.1	List of Runs . . . . .	58
A.2	Description of Angular Distributions . . . . .	61



# 1. Light Scalar Resonances

The human being has been interested in the investigation of composition and interaction of matter ever since. In the fifth century BC the Greek philosopher Democritus, e.g., was convinced that everything is built up of small particles called atoms<sup>1</sup> which differ from matter to matter. As discovered during the last century, this principle turned out to be partially correct.

Matter is indeed composed of small elementary particles. At the end of the 19<sup>th</sup> century, people thought those particles were the chemical elements. This assumption needed to be changed when J. J. Thomson discovered the electron in 1897, and E. Rutherford in the beginning of last century found out that almost the whole mass of atoms is concentrated in a tiny, positively charged nucleus. A few decades later, in 1932, the neutron was discovered by J. Chadwick. In the middle of last century particle accelerators were built and experiments there led to the discovery of a large number of different particles, sometimes called a “particle zoo”<sup>2</sup>, and the recognition that those particles are not indivisible but composed of so-called quarks<sup>3</sup>.

Our current picture of the composition and interaction of matter within the framework of the Standard Model is the following (see Table 1.1):

Matter is composed of elementary particles with half-integer spin quantum numbers (in units of  $\hbar$ ). These particles are called fermions and are subdivided into leptons and quarks. The forces between them are mediated by exchange bosons (particles with integral spin).

---

<sup>1</sup>atomos: Greek for indivisible

<sup>2</sup>I found a very nice citation of Enrico Fermi in Ref. [PDG86]: “Young man, if I could remember the names of these particles, I would have been a botanist.”

<sup>3</sup>The word ‘quarks’ has been suggested by M. Gell-Mann.

Fermions	Family	Electric Charge	Color	Spin
	1 2 3			
Leptons	$\nu_e \nu_\mu \nu_\tau$	0	–	1/2
	$e \mu \tau$	-1	–	1/2
Quarks	$u \ c \ t$	+2/3	{red, blue,	1/2
	$d \ s \ b$	-1/3	green}	1/2

Interaction	Couples to	Exchange Boson	Mass [GeV/c <sup>2</sup> ]	$J^P$
strong	Color	8 Gluons $g$	0	1 <sup>-</sup>
e-m	e-m Charge	Photon $\gamma$	0	1 <sup>-</sup>
weak	weak Charge	$W^\pm, Z^0$	80-90	1
Gravitation	Energy	Graviton $g$	0	2 <sup>+</sup>

Table 1.1: Upper part: The elementary particles with their properties. Each particle has a corresponding anti-particle with the same spin but opposite charge and anti-color. Lower part: The exchange bosons mediating the forces between interacting particles.

## 1.1 Baryons and Mesons

Quarks (labeled with the symbol  $q$ ) have never been observed as free particles but they combine to form other particles called hadrons. G. Zweig and M. Gell-Mann classified the hadronic states based on symmetry principles. The underlying symmetry groups led to the invention of quarks which were later identified in deep inelastic  $e^-$ -scattering as partons. According to this naive quark model all hadrons are built up of either  $q\bar{q}$  or  $qqq$ , the first being called mesons, the latter baryons.

Baryons are composed of three quarks. Their spins couple to either  $S = 1/2$  or  $S = 3/2$ . For simplicity let us consider states with the lowest masses only which means we assume zero relative angular momentum between the quarks. With this assumption the total angular momentum is equal to the sum of the spins of the three quarks. Using u, d and s quarks only and assuming the Pauli principle leads to a baryon octet for spin  $S = 1/2$  and to a decuplet for  $S = 3/2$  states. They are shown in Fig. 1.1. When these multiplets were introduced the  $\Omega^-$  had not yet been discovered. It was a great success when the particle was experimentally observed having the predicted quantum numbers and mass.

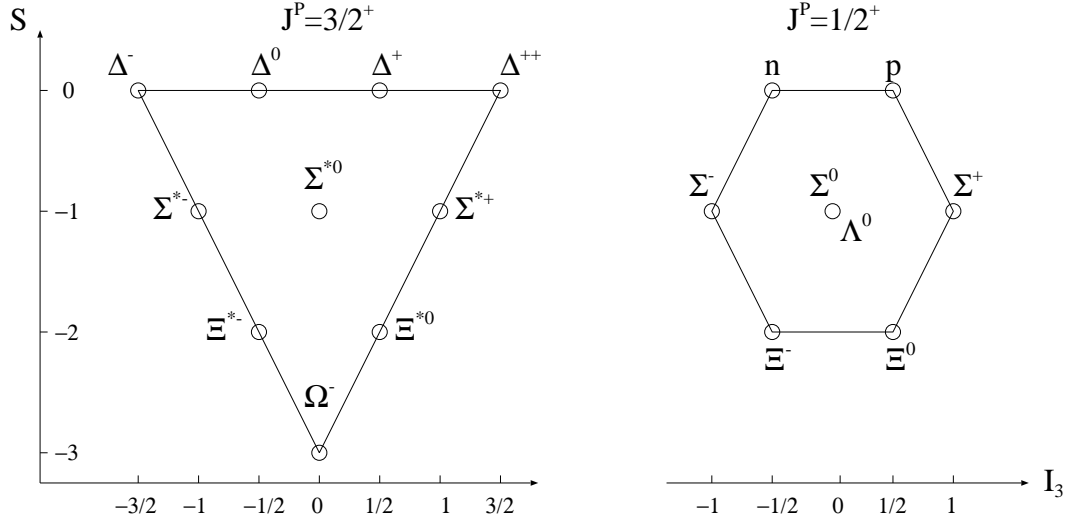


Figure 1.1: The lightest baryon decuplet and octet. The resonances in a multiplet differ in strangeness  $S$  and the third component of isospin  $I_3$ .

Mesons are composed of a  $q\bar{q}$  pair. Since quarks are fermions carrying spin  $S = 1/2$ , the  $q\bar{q}$  pair of a meson can couple to  $S = 0$  or  $S = 1$ . The total angular momentum is the sum of the angular momentum  $L$  between the  $q\bar{q}$  pair and its spin  $S$ ,  $J = L + S$ . Since fermions and anti-fermions have opposite parity, the parity is  $P = (-1)^{L+1}$ . Different combinations of  $J$  and  $P$  lead to different multiplets. For mesons with  $L = 0$  and 1 the combinations  $J^P = 0^-$  (pseudo-scalar mesons),  $J^P = 1^-$  (vector mesons),  $J^P = 0^+$  (scalar mesons),  $J^P = 1^+$  (axial mesons) and  $J^P = 2^+$  (tensor mesons) are possible. Restricting the quarks to u, d and s, leads to meson nonets. The well established nonet for pseudo-scalar mesons is shown in Fig. 1.2, left side.

### Scalar Mesons

In the case of low mass baryons, pseudo-scalar and vector mesons all states of the quark model have been identified with observed states. This is not the case for scalar mesons. More resonances have been observed in the expected mass range ( $m \approx 600 - 1900 \text{ MeV}/c^2$ ) than would fit into a single nonet. It is not clear up to now which of these are the genuine  $q\bar{q}$  states and what is the nature of the others. The difficulty of finding the candidates for the scalar nonet is dominated by the large decay width of these resonances as well as the fact that several decay channels open up within a short mass interval. Moreover, in the mass region of interest,

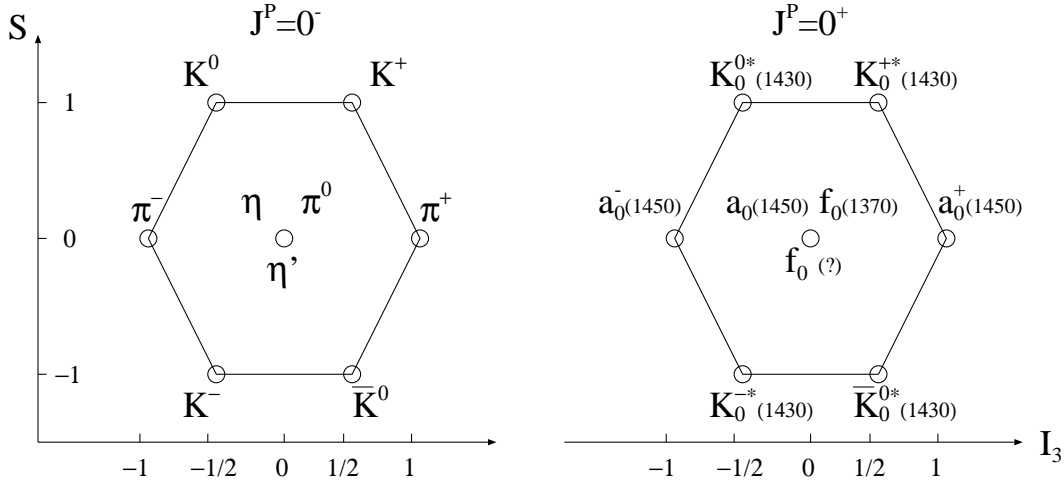


Figure 1.2: The nonet of pseudo-scalar mesons and of scalar mesons derived from the naive quark model [PDG02].  $S$  indicates the strangeness content, while  $I_3$  is the third component of isospin.

objects like glueballs ( $gg$  and  $ggg$ ) and multi-quark states ( $qq\bar{q}\bar{q}$  and  $qqq\bar{q}\bar{q}$ ) are expected [PDG02].

Candidates for the scalar nonet are the  $K^*(1430)$  with  $I = 1/2$ , the  $a_0(980)$  and  $a_0(1450)$  with  $I = 1$  and the  $\sigma$  or  $f_0(500)$ ,  $f_0(980)$ ,  $f_0(1370)$  and  $f_0(1500)$  with  $I = 0$ . The  $K^*(1430)$  is assumed to be a  $q\bar{q}$  state in almost every model. In the framework of the naive quark model the nonet would look as shown on the right side of Fig. 1.2 whereas the ninth member is ambiguous. It could, for example, be the  $f_0(1500)$  or  $f_0(1710)$  [PDG02].

This is only one possibility to group the scalar nonet. Many theoretical models were developed but none of them is able to describe the scalar sector satisfactory [Büs02b]. The two resonances  $a_0(980)$  and  $f_0(980)$  have a mass near  $980 \text{ MeV}/c^2$  where the  $a_0(980)$  has been observed in three charge states ( $\pm 1, 0$ ) and the  $f_0(980)$  is neutral. In some relativistic quark models the  $a_0(980)/f_0(980)$  are considered as  $q\bar{q}$  states [Ric00, Cel00, Ani00, Nar01], whereas Refs. [Cel00, Ani00, Nar01] deduce a glueball mixing with the  $q\bar{q}$  states in order to reproduce the observed states.

Other models prefer to describe the  $a_0(980)/f_0(980)$  as tetraquark states [Vij02, Clo92] or mesonic molecules [Wei83, Loh90]. Within the framework of chiral perturbation theory a model has been developed in which the  $a_0(980)/f_0(980)$  are dynamically generated bound states of two mesons [Oll00, Ose01].

From the diversity of theoretical models it becomes clear that the field of scalar resonances is not settled at present and new data are necessary.

## 1.2 Experiments on the $a_0(980)$ Resonance

The first evidence for the existence of the  $a_0(980)$  resonance has been provided in the late 60s. At that time three resonances were observed, called  $\delta(962)$ ,  $\pi_N(975)$  and  $\pi_N(1016)$ . The first two were observed in  $\pi\eta$  systems, the latter in  $K\bar{K}$  final states. Over the years the  $\delta(962)$  was discarded and it turned out that the  $\pi_N(975)$  and  $\pi_N(1016)$  are of the same origin. This resonance was first renamed as  $\delta(980)$  and later as  $a_0(980)$  ([PDG69, PDG71, PDG73, PDG80, PDG86]). The absence of a  $\rho\pi$  decay was a strong indication that its spin is zero ( $S = 0$ ) and its parity positive ( $P = +1$ ). Flatté [Fla76] proposed that the  $\pi\eta$  and  $K\bar{K}$  invariant mass spectra can be reasonably explained by a two-channel resonance of large width which is narrowed due to unitarity and analyticity. An example for such a Flatté distribution is shown in Fig. 1.3.

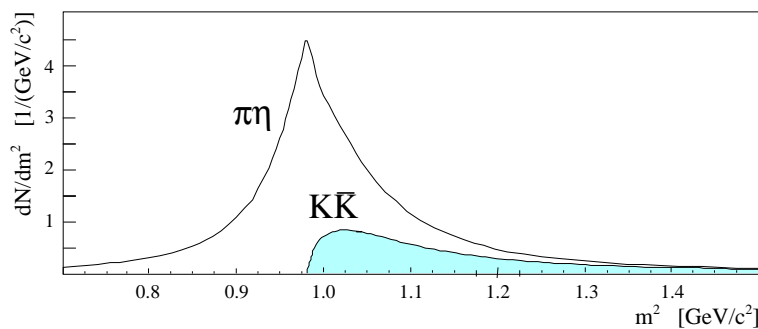


Figure 1.3: Possible Flatté distribution for the  $a_0(980)$  decay channels  $\pi\eta$  and  $K\bar{K}$ . The parameters used for the calculation are described in Ref. [Bra02].

Since then, many experiments have been performed in which the  $a_0(980)$  resonance was observed. In this section an overview of the various experiments is given (Table 1.3). The overview is far from being complete. Mainly those experiments were chosen where the results are accepted by the Particle Data Group [PDG02]. From all these measurements the mass of the  $a_0(980)$  is known quite well ( $984.7 \pm 1.2 \text{ MeV}/c^2$ ). The width is only estimated ( $\Gamma = 50$  to  $100 \text{ MeV}$ ) although about as many values have been published as for the mass. Only very few experiments give a branching ratio of the decay channels  $\pi\eta$  and  $K\bar{K}$  and have been accepted to generate an average value. Almost all measurements were performed at high energies where the  $a_0(980)$  is observed as a decay product of higher lying resonances. One of the experiments listed in Table 1.3 provides cross sections on  $a_0(980)$  production [Abo70] and only three were performed in  $pp$  collisions [Abo70, Bar00, Bar98]. In spite of these many experiments the information available is not yet sufficient

to reveal the nature of the  $a_0(980)$  resonance. Thus, with the experimental program on the investigations of the  $a_0^+(980)$  resonance with ANKE at COSY–Jülich we want to provide additional and complementary information. The broader goal of the scientific program is to study  $a_0(980)/f_0(980)$  production in  $pp$ ,  $pn$ ,  $pd$  and  $dd$  interactions [Büs02b]. Both decay channels,  $a_0 \rightarrow K\bar{K}/\pi\eta$  and  $f_0 \rightarrow K\bar{K}/\pi\pi$  can be detected simultaneously. The  $a_0(980)/f_0(980)$  are observed in direct production, i.e. not via the decay of higher lying resonances. Angular and mass distributions and total cross sections will be provided.

The first two experiments of the ANKE program on scalar resonances have been performed in  $pp$  collision at  $T_p = 2.65$  GeV and 2.83 GeV where the  $a_0^+(980)$  is produced in coincidence with a deuteron,  $pp \rightarrow da_0^+(980) \rightarrow dK^+\bar{K}^0/d\pi^+\eta$ . The  $\pi^+\eta$  as well as the  $K^+\bar{K}^0$  decay channel have been measured simultaneously. In this thesis the analysis of coincident  $dK^+$  pairs of the first beamtime at  $T_p = 2.65$  GeV is described.

### 1.3 $pp \rightarrow da_0^+ \rightarrow dK^+\bar{K}^0$ near Threshold

At  $T_p = 2.65$  GeV the reaction  $pp \rightarrow da_0^+ \rightarrow dK^+\bar{K}^0$  is  $Q = 46$  MeV above the  $K\bar{K}$  production threshold. The proximity to the threshold and the quantum numbers of the final state impose strong constraints on the angular distributions. Final states with zero angular momenta everywhere are forbidden while at  $Q = 46$  MeV partial waves higher than  $l = 1$  are suppressed.

The final state is formed by two particles with the quantum numbers  $J^P = 0^+$  ( $a_0$ ) and  ${}^{2S+1}L_J = {}^3S_1$  (deuteron). In the following, some restrictions on the final and initial states are derived, using the Pauli Principle and the conservation laws on angular momentum and parity.

The lowest possible relative angular momentum between the deuteron and the  $a_0$  is  $l = 0$  which means that the total angular momentum  $J$  and the parity  $P$  of the final state is  $J = 1$  and  $P = (-1)^l \cdot (+1)_{a_0} \cdot (+1)_d = +1$ . The next higher partial wave is  $l = 1$  and thus  $J = 0, 1, 2$  and has negative parity  $P = -1$ . Higher partial waves are possible but kinematically suppressed due to the nearness of the  $K^+\bar{K}^0$  threshold.

The initial channel contains two protons with the quantum numbers  $J^P = 1/2^+$  each. Using the Pauli Principle, the wave function of the system must be antisymmetric which means that  $(-1)^{L+S+I}$  has to be negative. The isospin of two protons is  $I = 1$  ( $I_3 = 1/2 + 1/2 = 1$ ). The wave function is anti-symmetric, if the sum of the angular momentum and the spin of the two protons  $L + S$  is even where the spin  $S$  can be 0 and 1.

A final state with positive parity can be produced, if the angular momentum of the two protons  $L$  is even ( $P = (-1)^L$ ,  $L = 0, 2, \dots$ ) which implies the even spin quantum number  $S = 0$  and therefore  $J = L$ . However, as shown above, there is no final state close to threshold with these quantum numbers. Therefore, a final state with  $l = 0$

between all particles is forbidden.

Final states with negative parity can be produced with odd angular momenta ( $L = 1, 3, \dots$ ) and spin  $S = 1$ . The total angular momentum of the two protons  $J$  has to be either  $J = 0, 1, 2$  in order to fulfill angular momentum conservation. This means that the final state containing a  $p$ -wave can only be produced from  ${}^3P_{0,1,2}$  and  ${}^3F_2$  initial states.

Experimentally observed at ANKE are the deuteron and the  $K^+$  meson. The missing  $\overline{K}^0$  is reconstructed. Thus, the  $K\overline{K}$  can also be produced without an  $a_0$  involved. In the case of non-resonant  $dK^+\overline{K}^0$  production, analogous arguments as above lead to the condition that the observed  $dK^+\overline{K}^0$  events must have a relative  $P$ -wave distribution in one of the systems  $K^+\overline{K}^0$  or  $d(K^+\overline{K}^0)$ , the latter would be the identical configuration as for  $a_0^+$ -production. We denote the state where the deuteron is in a  $p$ -wave ( $s$ -wave) relative to the  $K^+\overline{K}^0$  system and the  $K^+\overline{K}^0$  system itself in a relative  $S$ -wave ( $P$ -wave) as  $Sp$  ( $Ps$ ).

Collaboration (and/or) Detector	Facility	Beam Energy [GeV/c]	Reaction	Selected ( $a_0(980)$ ) Events	Mass [MeV/c <sup>2</sup> ]	Width [MeV]	Branching Ratio $a_0(980) \rightarrow$ $K\bar{K}/\pi\eta$	Method	Ref.	Year (publ.)
PDG					$948.7 \pm 1.2$	50 to 100	$0.177 \pm 0.024$	compilation	[PDG02]	2002
L3	LEP <sup>a</sup>	$183 \leq \sqrt{s} \leq 209$	$e^+e^- \rightarrow e^+e^-\gamma\gamma$ $\rightarrow e^+e^-f_1(1285)$ $\rightarrow e^+e^-\eta\pi^+\pi^-$	11254 (313)	$985 \pm 4$ $\pm 6$	$50 \pm 13$ $\pm 4$	-	fit of inv. mass	[Arc02]	2002
WA102 Omega GAMS-4000	CERN	450	$pp \rightarrow p_s(\eta\pi^0)pf$ $\rightarrow p_s(4\gamma)pf$ $pp \rightarrow p_s(\eta\pi^-)\Lambda^{++}$ $\rightarrow p_s(2\gamma\pi^-)pf$	6045  8027	$975 \pm 7$  $988 \pm 8$	$72 \pm 16$  $61 \pm 19$	-	fit of inv. mass + PWA <sup>b</sup> fit of inv. mass + PWA <sup>b</sup>	[Bar00] [Bar00]	2000
E852 MPS <sup>d</sup> LGDF <sup>f</sup>	AGS <sup>c</sup> BNL <sup>e</sup>	18.3	$\pi^-p \rightarrow \eta\pi^+\pi^-n$ $\pi^-p \rightarrow \eta\pi^0n \rightarrow 4\gamma n$	(1318) (1320)	$993.1 \pm 2.1$	$71 \pm 7$	-	fit of inv. mass + PWA <sup>b</sup>	[Tei99]	1998
WA102 OMEGA GAMS-4000	CERN	450	$pp \rightarrow p_s(\eta\pi^+\pi^0)pf$ $\rightarrow p_s(2\gamma\pi^+\pi^-)pf$ or $\rightarrow p_s(2\pi^+2\pi^-2\gamma)pf$	90393	-	-	$0.166 \pm 0.01$ $\pm 0.02^g$ via $f_1(1285)$	spin-parity analysis	[Bar98]	1998
OBELIX	LEAR CERN	annihil. at rest	$\bar{p}p \rightarrow K^\pm K_s^0\pi^\pm$	42000	$975 \pm 15$	$65 \pm 10$	-	spin parity analysis	[Ber98]	1998
Crystal Barral	LEAR CERN	annihil. at rest	$\bar{p}p \rightarrow K_L^0 K^\pm\pi^\pm$	12000 $\pm 600$	$982 \pm 3$	$92 \pm 8$	$0.23 \pm 0.05^h$	PWA	[Abc98]	1998
Crystal Barral	LEAR CERN	annihil. at rest	$\bar{p}p \rightarrow \omega\eta\pi^0$ $\rightarrow \pi^0\eta\pi^0 \rightarrow 7\gamma$	106662 $\pm 268$	$984.45 \pm 1.23$ $\pm 0.34$	$54.12 \pm 0.34$ $\pm 0.12$	-	fit of inv. mass	[Ams94a]	1994
Crystal Barral	LEAR CERN	annihil. at rest	$\bar{p}p \rightarrow \eta\eta\pi^0$ $\rightarrow 6\gamma$	22492	$982 \pm 2$	$54 \pm 10$	-	fit of inv. mass	[Ams92]	1992



Collaboration (and/or) Detector	Facility	Beam Energy [GeV/c]	Reaction	Selected ( $a_0(980)$ ) Events	Mass [MeV/c <sup>2</sup> ]	Width [MeV]	Branching Ratio $a_0(980) \rightarrow$ $K\overline{K}/\pi\eta$	Method	Ref.	Year (publ.)
Jade	PETRA DESY	av. 18	$e^+e^- \rightarrow e^+e^-\gamma\gamma$ $\rightarrow e^+e^-\pi^0\eta$ $\rightarrow e^+e^-4\gamma$	291 (44 ± 7)	-	-	$_{-i}$	fit of inv. mass	[Oes90]	1990
Crystal Ball	DORIS II DESY	4.7 - 5.3	$e^+e^- \rightarrow e^+e^-\gamma\gamma$ $\rightarrow e^+e^-\pi^0\eta$ $\rightarrow e^+e^-4\gamma$	336	1005 ± 9	$32 \pm_{32}^{50}$	$_{-j}$	fit of inv. mass	[Ant86]	1986
Omega Photon WA57	SPS <sup>k</sup> CERN	22-55	$\gamma p \rightarrow X$	5000000	976 ± 6	-	-	fit of inv. mass	[Atk84]	1984
Omega Spectrometer	CERN	12	$\pi^-p \rightarrow X^-p$	1270000 (ca.500)	986 ± 3	62 ± 15	-	fit of inv. mass	[Eva81]	1981
2m Bubble Chamber	CERN	1.2-2.04	$\overline{p}p \rightarrow f_1(1285)\omega$ $\rightarrow K_1^0 K^\pm \pi^\mp \pi^+ \pi^- \pi^0$	1296 ± 23 (316 ± 23)	970 ± 10	-	-	fit of inv. mass	[DeB80]	1980
ACNO <sup>l</sup> 2m Bubble Chamber	CERN	4.2	$K^-p \rightarrow \Lambda_1^-(1285)$ $\rightarrow \Lambda\eta\pi^+\pi^-$	72162 (145 ± 25)	990 ± 7	60 ± 20	-	fit of inv. mass	[Gur79]	1979
ABCCCHW <sup>m</sup> 2m Bubble Chamber	PS <sup>n</sup> CERN	16	$\pi^-p \rightarrow p6\pi$ $\pi^+p \rightarrow p\pi^+(K\overline{K}\pi)^0$	24902 (115)	977 ± 7 -	44 ± 22 -	>0.08 (estimate)	fit of inv. mass	[Gra77]	1977
81 cm HBC <sup>o</sup>	CERN	0.72	$\overline{p}p \rightarrow 3\pi^+3\pi^-\pi^0$	75000 (ca.282)	972 ± 10	30 ± 5	0.25 ± 0.08 <sup>q</sup>	estimates	[Def72]	1972
wire spark chamber + deuteron spectrometer	Bevatron LRL <sup>p</sup>	3.8, 4.5, 6.3 <sup>q</sup>	$pp \rightarrow dX$	630000	975 ± 6	60 ± $_{10}^{16}$		fit of missing mass	[Abo70]	1970

- <sup>a</sup> Large Electron Positron Collider  
<sup>b</sup> Partial Wave Analysis  
<sup>c</sup> Alternating Gradient Synchrotron  
<sup>d</sup> Multiple Particle Spectrometer  
<sup>e</sup> Brookhaven National Laboratory  
<sup>f</sup> Lead Glass Detector  
<sup>g</sup> via  $f_1(1285)$  and using Refs. [Bar97b, Bar97a]  
<sup>h</sup> Using  $\pi^0\pi^0\eta$  from Ref. [Ams94b]  
<sup>i</sup>  $\Gamma(\pi\eta) \times \Gamma(\gamma\gamma)/\Gamma(\text{total}) = (0.28 \pm 0.04 \pm 0.10)$  keV  
<sup>j</sup>  $\Gamma(\pi\eta) \times \Gamma(\gamma\gamma)/\Gamma(\text{total}) = (0.28 \pm 0.04 \pm 0.10)$  keV
- <sup>k</sup> Super Proton Synchrotron  
<sup>l</sup> Amsterdam - CERN - Nijmegen - Oxford  
<sup>m</sup> Aachen - Berlin - Bonn - CERN - Cracow - Heidelberg - Warsaw  
<sup>n</sup> Proton Synchrotron  
<sup>o</sup> Hydrogen Bubble Chamber  
<sup>p</sup> Lawrence Radiation Laboratory  
<sup>q</sup> From this experiment cross sections have been determined:  
 $\frac{d\sigma}{d\Omega}(pp) = 3.8 \text{ GeV}/c = 0.50 \pm 0.70 \frac{\mu\text{b}}{\text{sr}}$ ,  
 $\frac{d\sigma}{d\Omega}(pp) = 4.5 \text{ GeV}/c = 0.48 \pm 0.28 \frac{\mu\text{b}}{\text{sr}}$ ,  
 $\frac{d\sigma}{d\Omega}(pp) = 6.3 \text{ GeV}/c = 0.35 \pm 0.19 \frac{\mu\text{b}}{\text{sr}}$

## 2. ANKE-Experiment on $a_0^+$ (980) production

### 2.1 The ANKE Spectrometer at COSY–Jülich

The Cooler Synchrotron COSY–Jülich [Mai97] is designed to provide unpolarized and polarized proton and deuteron beams in the momentum range of 294 - 3650 MeV/c. Ions from a  $H^-$  ( $D^-$ ) source are pre-accelerated with the cyclotron JULIC to an energy of 45 MeV (76 MeV) and injected into the 184 m long COSY ring via a charge exchanging stripper foil. The ions are accelerated to the desired energy with a cavity while 24 dipole and 56 quadrupole magnets keep them on the track and focus them. Electron and stochastic cooling guarantee high quality beams with small emittance and momentum spread which can be used for internal and external experiments.

Currently, four internal experiments are installed, ANKE [Bar01], COSY11 [Bra96], EDDA [Alb97] and PISA [PIS99]. COSY–11 aims at studying near threshold meson production. EDDA has investigated elastic proton–proton scattering from  $T_p = 0.5$  to 2.5 GeV with high precision using unpolarized and polarized beams and targets. PISA is used to investigate total and differential cross sections of proton induced spallation from several targets, the results being important for the planning and construction of the European Spallation Source ESS [Cla01].

Five external experiments use the extracted COSY beam, GEM [Bet99], JESSICA [Tie01], MOMO [Bel99], NESSI [Enk99] and TOF [Boh00]. JESSICA serves as a test facility to investigate spallation targets and moderators whereas NESSI provides precision data for neutrons and charged particles in proton induced spallation. GEM as well as MOMO are used in conjunction with the BIG KARL spectrometer. MOMO was designed to study the reactions  $pd \rightarrow {}^3\text{He}K^+K^-/\pi^+\pi^-$  near threshold, GEM to study meson production near threshold. With the large acceptance time-of-flight spectrometer TOF mainly meson and hyperon production is investigated, also far above the production thresholds.

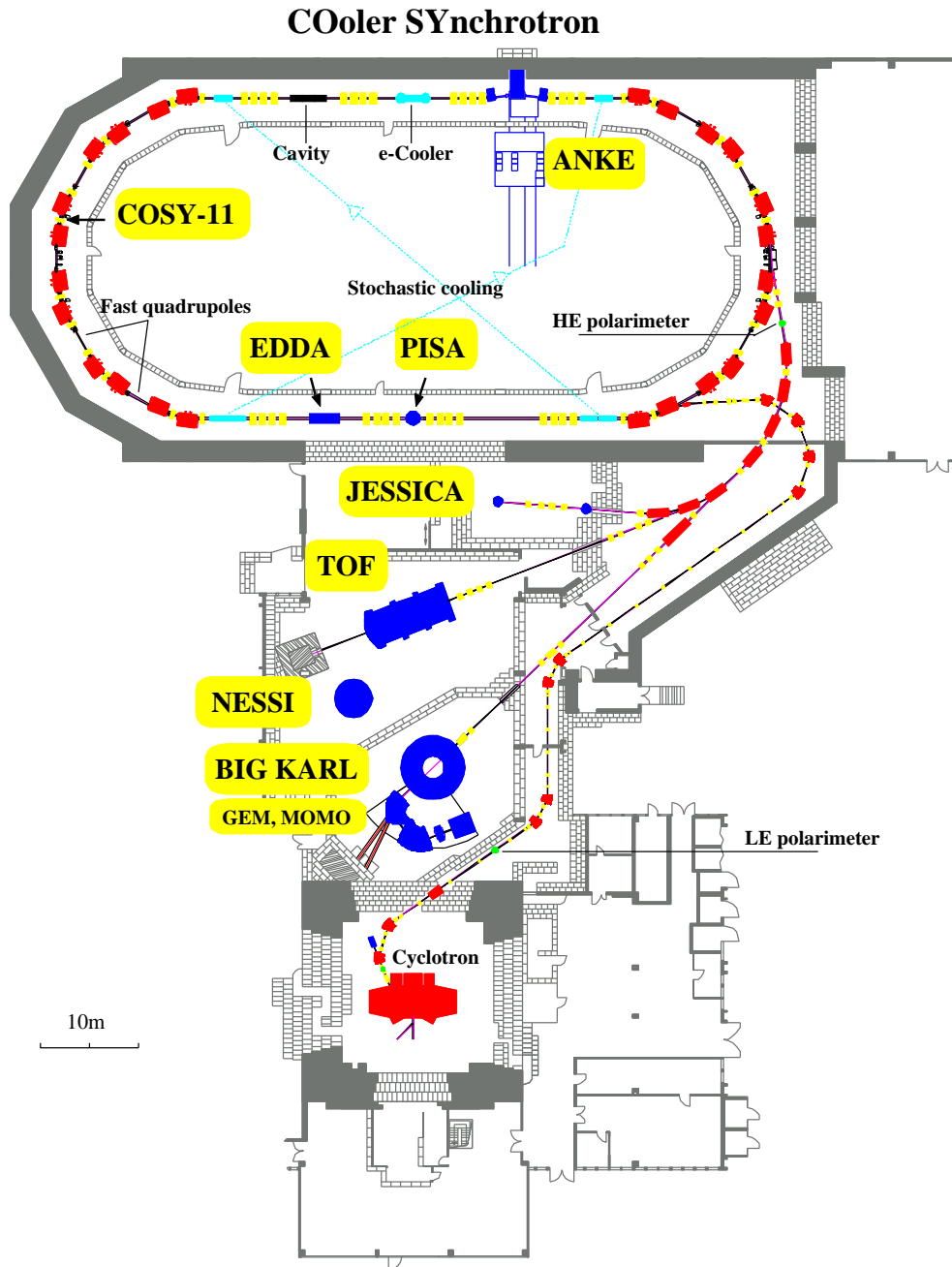


Figure 2.1: The Cooler Synchrotron COSY.  $H^-$  and  $D^-$ -Ions are pre-accelerated in the cyclotron JULIC and injected into the COSY ring via a charge exchanging stripper foil. At present, four internal experiments are installed (ANKE, COSY-11, EDDA and PISA) and five external (JESSICA, TOF, NESSI and GEM and MOMO at BIG KARL).

The Apparatus for Nucleon and Kaon Ejectiles ANKE is an internal spectrometer for charged particles at COSY–Jülich. It has been put into operation in spring 1998 and is optimized for the study of subthreshold  $K^+$  production from nuclei. This requires the identification of kaons in an immense background of pions and protons. Thus, a dedicated detection system has been developed [Büs02a] which could be used within the framework of this thesis guaranteeing an excellent kaon identification. In the following the layout of ANKE is briefly described. Detailed information can be found in Ref. [Bar01].

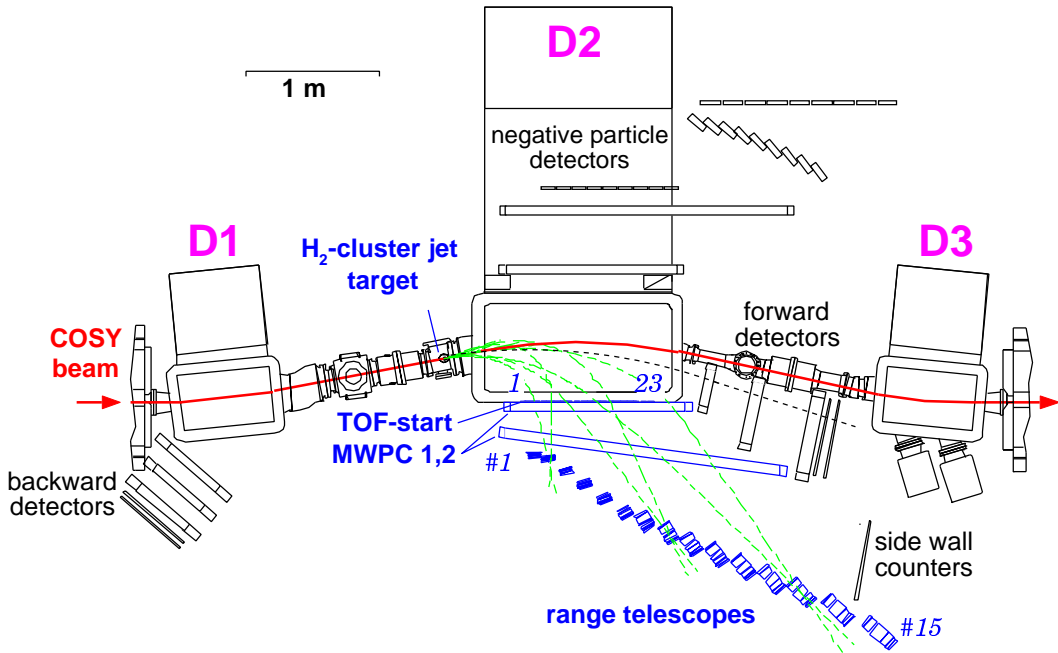


Figure 2.2: Sketch of the ANKE spectrometer and its detection systems. Forward emitted positively charged particles can be detected in the side and forward detection system. A detection system for negatively charged particles has been built. For backward emitted particles the backward detection system is available. Measurements can be done from cluster and strip targets. In this measurement the cluster target was used together with the side and forward detection system. The dashed curves indicate particle trajectories.

ANKE (see Fig. 2.2) consists of three dipole magnets D1, D2 and D3. D2 is used as spectrometer magnet for forward emitted ejectiles from the target placed in front of D2 while D1 and D3 guide the circulating COSY beam. The deflection angle of the beam  $\alpha_{D1} = \alpha_{D3} = -1/2 \cdot \alpha_{D2}$  can be adjusted to optimize the magnetic field independent on the COSY beam momentum. Various targets can be used, H<sub>2</sub>- or D<sub>2</sub>-cluster jets [San97] or strip targets made of, e.g. C, Cu, Ag and Au [Bar01]. Moreover, a frozen pellet target [Bou98] is in preparation providing highest luminosities

for  $H_2$  and  $D_2$  which are comparable those achieved with strip targets. An Atomic Beam Source (ABS) [Mik02] will be installed in the near future for measurements with polarized H and D targets.

Positively charged forward emitted particles are detected with the side and forward detection system (FDS/SDS) described in the next sections. A detection system for negatively charged particles has been built [Har01], TOF start and stop counters and two MWPCs have already been installed and put into operation.

Moreover, backward emitted particles are identified with the backward detection system (BDS) comprising three drift chambers and two layers of scintillators [Bar01]. D1 is then used as a spectrometer magnet.

A near-target spectator detector [Leh00] is available in order to perform measurements on deuterium as an effective neutron target, tagging the spectator protons. A photon detector [Hej02] is in preparation which will allow the detection of photons as well.

## 2.2 Experimental Setup

The measurement on  $a_0^+$  production was performed in two weeks in the beginning of 2001. The general idea of the measurement is to study the reactions  $pp \rightarrow da_0^+(980) \rightarrow dK^+\bar{K}^0/d\pi^+\eta$  by detecting the deuteron in the forward detection system and the charged  $a_0^+$  decay product in the side detection system. A missing mass analysis of the experimentally observed coincident  $dK^+/d\pi^+$  events allows one to identify events from the reaction  $pp \rightarrow dK^+\bar{K}^0/d\pi^+\eta$ . In this thesis, only the analysis of  $dK^+X$  events is described. The  $\pi^+\eta$  channel is analyzed independently [Fed02]. In the following the experimental conditions and those parts of ANKE are described which were used for the measurement on  $a_0^+$ -production.

### 2.2.1 COSY Beam, Target and Magnetic Field

In the beginning of the beamtime calibration measurements at  $T_p = 0.5, 0.7$  and  $1.0$  GeV and a beam deflection angle of  $\alpha = 7.4^\circ$  have been performed, corresponding to magnetic field values in D2 of  $B = 0.605, 0.746$  and  $0.945$  T. During the experiment at  $T_p = 2.65$  GeV up to  $4 \cdot 10^{10}$  protons with a cycling frequency of about 1.58 MHz were provided by COSY. Together with the  $H_2$ -cluster jet target (dimensions:  $\sim 5$  mm in transversal, 12 mm in longitudinal direction) which reached cluster densities of up to  $5 \cdot 10^{14}$  cm $^{-2}$  an average luminosity of  $2 - 3 \cdot 10^{31}$  cm $^{-2}$ s $^{-1}$  could be obtained. The magnetic field of D2 was set to 1.57 T at an ANKE deflection angle of  $\alpha = 5.9^\circ$ .

### 2.2.2 The Side Detection System (SDS)

The detection system for forward emitted charged particles is subdivided into a low (SDS) and high momentum part (FDS). The SDS covers the momentum range of 150 - 1100 MeV/c. With the settings described above, ejectiles with horizontal angles in the range  $\pm 12^\circ$  and a vertical angle of  $\pm 3.5^\circ$  pass one of the 23 time-of-flight (TOF) start counters behind the side exit window of D2 and are focused onto one of the 15 range telescopes or hit one of the 6 sidewall scintillation counters. The range telescopes are placed in the focal plane of D2, each covering a momentum interval of roughly 30 MeV/c. The general layout of a telescope is shown in Fig. 2.3.

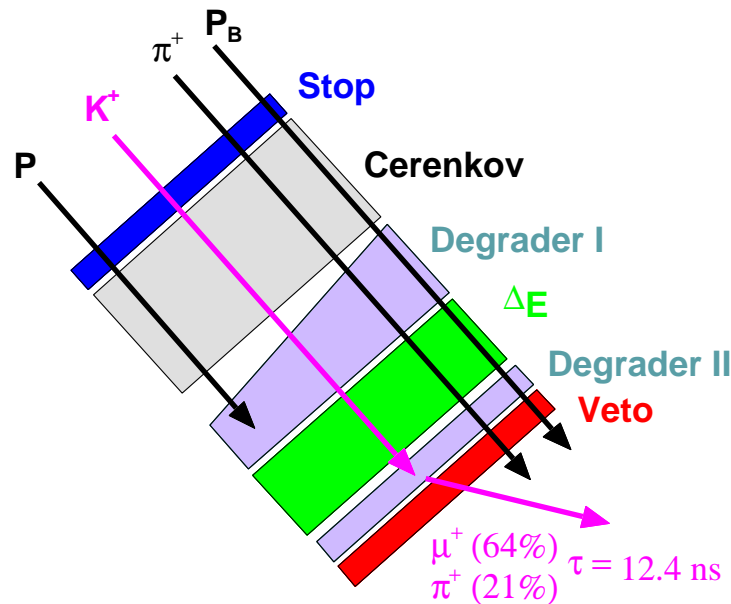


Figure 2.3: Sketch of an ANKE telescope. It is composed of a stop, Cerenkov (in telescopes 7 - 15 only),  $\Delta E$  and veto scintillator and two degraders. The degraders are designed such that protons are stopped in the first and  $K^+$  mesons in the second. Kaon decay products are observed in the veto counter with characteristic delay time.

The most important information used to discriminate particles in the SDS is the TOF between the start and the stop counters. A lucite Cerenkov counter follows the plastic stop counter in order to identify pions via their light emission. Since the pions need to have a momentum of more than 300 MeV/c to produce a signal in the Cerenkov counters, those are used in telescopes 7 to 15 only.

The next part is a degrader built of copper which stops protons stemming from the

target and decelerates the kaons so that they just pass the following  $\Delta E$  counter and are stopped in the second degrader. There they decay with the lifetime of 12.4 ns. Detecting the kaon decay products  $\mu^+$ ,  $\pi^+$  by requiring a delayed signal in the last counter (veto), after the  $\Delta E$  counter has been hit, is a strong criterion to select kaons. However, it implies a reduction of the efficiency by a factor of 7 - 8 due to the limited solid angle for detecting the decay products. Therefore, it has only been used off-line to identify the kaon signals clearly. At  $T_p = 2.65$  GeV kaons in the telescopes 10 - 15 can be identified by means of TOF and energy loss only. Pions still are minimum ionizing and pass all detectors.

In order to measure particles with higher momenta (625 - 1100 MeV/c) as well, the sidewall has been set up which is composed of six scintillation counters. The first counter is placed next to telescope 15 and the wall is inclined so that the penetrating particles hit the scintillation counter perpendicularly. The scintillator thickness of 10 mm polystyrene is not sufficient to identify kaons via energy loss but pion and proton identification is easily possible via TOF. Thus, the sidewall has been used to identify pions from the reaction  $pp \rightarrow d\pi^+X$ .

For kaon identification only telescopes 10 - 15 have been used in the present analysis. According to simulations those telescopes cover the lower momentum half of the momentum distribution of  $a_0^+$  decay kaons.

Two multiwire proportional chambers are placed between the start counters and the telescopes to suppress background and for momentum reconstruction. Each wire chamber has three wire planes, one with vertical wires, the other two with a wire inclination of  $\pm 30^\circ$ . A more detailed description of the chambers, the decoding and the chamber analysis can be found in Ref. [Jun00].

### 2.2.3 The Forward Detection System (FDS)

For  $B = 1.57$  T, particles with momenta in the range of 950 - 3463 MeV/c with a horizontal angle of  $\pm 10^\circ$  depending on the momenta and a vertical angle of  $\pm 3^\circ$  are detected in the FDS. The FDS consists of three multiwire proportional chambers (MWPCs) for background suppression and track reconstruction and a scintillator hodoscope.

Each chamber has two wire planes with horizontally and vertically arranged wires with a distance of 1 mm and two planes with strips inclined at  $\pm 18^\circ$  with respect to the wires. For the analysis described below, only the wire planes were taken into account.

The hodoscope is split into two parts, the first is a layer of 8 polystyrene scintillator counters, the second comprises 9 counters. The counters in layer 1 and 2 which are closest to the beam pipe are denoted as counter 1. For a more detailed description see Refs. [Bar01] and [Kom02].



### 2.2.4 Hardware Trigger and Data Acquisition

All SDS scintillation counters (start, stop,  $\Delta E$ , veto and sidewall) are read out at both ends via photomultipliers. So called "meantimers" generate the hardware mean of the time signals of both photomultipliers. Especially built modules for each stop counter allow one to set an individually adjustable TOF gate per telescope in coincidence with maximum 16 corresponding start counters. Based on the meantimer information and the hit start–stop coincidence, these trigger modules decide within 100 ns whether an event is accepted or not. The time-of-flight (TOF) distributions between the valid start counters and stop counter 11 are shown in Fig. 2.4 as an example. In all spectra a peak from pions is observed; in some of them a second peak from protons is seen as well. The limits of these TOF distribution reflect the length of the hardware trigger gate. It was chosen such that protons are just cut off in order to only record events with a pion or kaon in the SDS. The trigger rates for protons are almost as high as for pions and would only increase the deadtime of the system. There are only some spectra with a proton peak still within the gates.

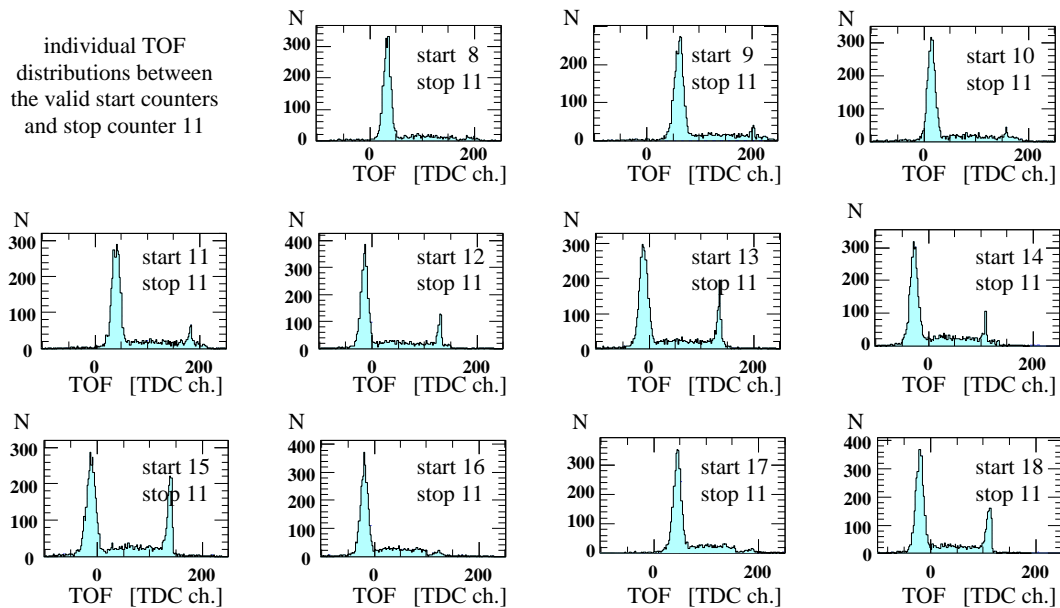


Figure 2.4: The trigger gate for the SDS has been adjusted to generate a trigger for pions (prominent peak) and kaons and to reject protons. Only in some start–stop counter combinations the proton peak is still seen at the end of the TOF gate.

The information on energy loss in the  $\Delta E$  counter can be included as well but has not been used online for this experiment.

The readout of the FDS scintillators is the same as the one in the SDS. A trigger signal was generated when a hodoscope of the first layer or one of the second layer was hit. (In the analysis, a hit in both layers was demanded.)

At ANKE four different triggers can be implemented simultaneously. During the  $a_0^+$  beamtime in most of the runs the main trigger  $T1$  was a coincidence between the SDS and FDS trigger. As second trigger  $T2$ , the trigger from the FDS alone, prescaled by a factor of 999, was chosen while the third trigger  $T3$  came from the SDS alone, prescaled by 200. Calibration runs with FDS and SDS trigger as non-prescaled main triggers were taken in addition. The fourth trigger is used to read out the scaler information for all scintillation counters.

In order to investigate events with coincident  $dK^+$  or  $d\pi^+$  pairs, the data which were recorded using trigger  $T1$  have been analysed. Data from trigger  $T2$  has been used to determine the luminosity and tune the forward system. With the data from trigger  $T3$ , the momentum reconstruction of the side system has been adjusted.  $T4$  can be used for deadtime corrections.

Using synchronised single board PCs the time to read out an event is about  $100 \mu s$ . The data are transmitted in clusters of subevents to the event builder. After the event builder, the information is written to DLT tapes and put at the disposal of online data analysis. Typical trigger rates were 5000 - 8500 events per second. The data acquisition was able to write about 1800 - 2700 events per second on tape, resulting in an average deadtime of about 50 - 30%.

Up to 80 GB can be stored on each DLT tape. During this measurement 25 tapes were written. The first 12 tapes contain calibration data and data where not all detectors were working well. The last 13 tapes have been used for this analysis containing 66 useful runs with about 10 million events each. A list of the runs and trigger conditions can be found in App. A.1.

## 3. Identification of $K^+$ Mesons

In this chapter the identification of  $K^+$  mesons is described. For the analysis they are selected by their time-of-flight between the start and stop counters and their energy-losses in the stop and  $\Delta E$ -scintillators. The most powerful selection criterion, the identification of kaons by their delayed decay products is only used to find and verify the time-of-flight and  $\Delta E$  selection. In the final analysis this criterion is not used since it reduces the statistics significantly and it is shown that  $K^+$  mesons can be identified by TOF and energy loss alone.

### 3.1 Time-of-Flight and Energy-Loss Information

The first step in the data analysis is to study the raw spectra (i.e. non-calibrated spectra). These contain all the information from the scintillation counters of events accepted by the hardware trigger without any additional selection criteria. In Fig. 3.1 the spectra of start counter 14 and stop and  $\Delta E$  counter 11 are shown as an example. The same raw spectra exist for all 23 start and the 15 stop and  $\Delta E$  counters.

The figures contain the energy losses and timing from the upper and lower photomultiplier, and the corresponding mean value. In the case of energy loss, the mean value is calculated by software while for the timing signal this is conveyed by hardware meantimers.

The energy loss distributions derived from the individual upper and lower photomultipliers are broad. Summing these two signals minimises the broadening effect due to the position dependent light-attenuation in the up to 1 m long scintillators. With the same amplification of both photomultipliers one observes an approximately linear correlation between the deposited energy and the QDC-signal, independent of the hit position in the scintillator. All information is given in QDC channels. An absolute calibration is not necessary since the selection of kaons is performed relative to pions and protons.

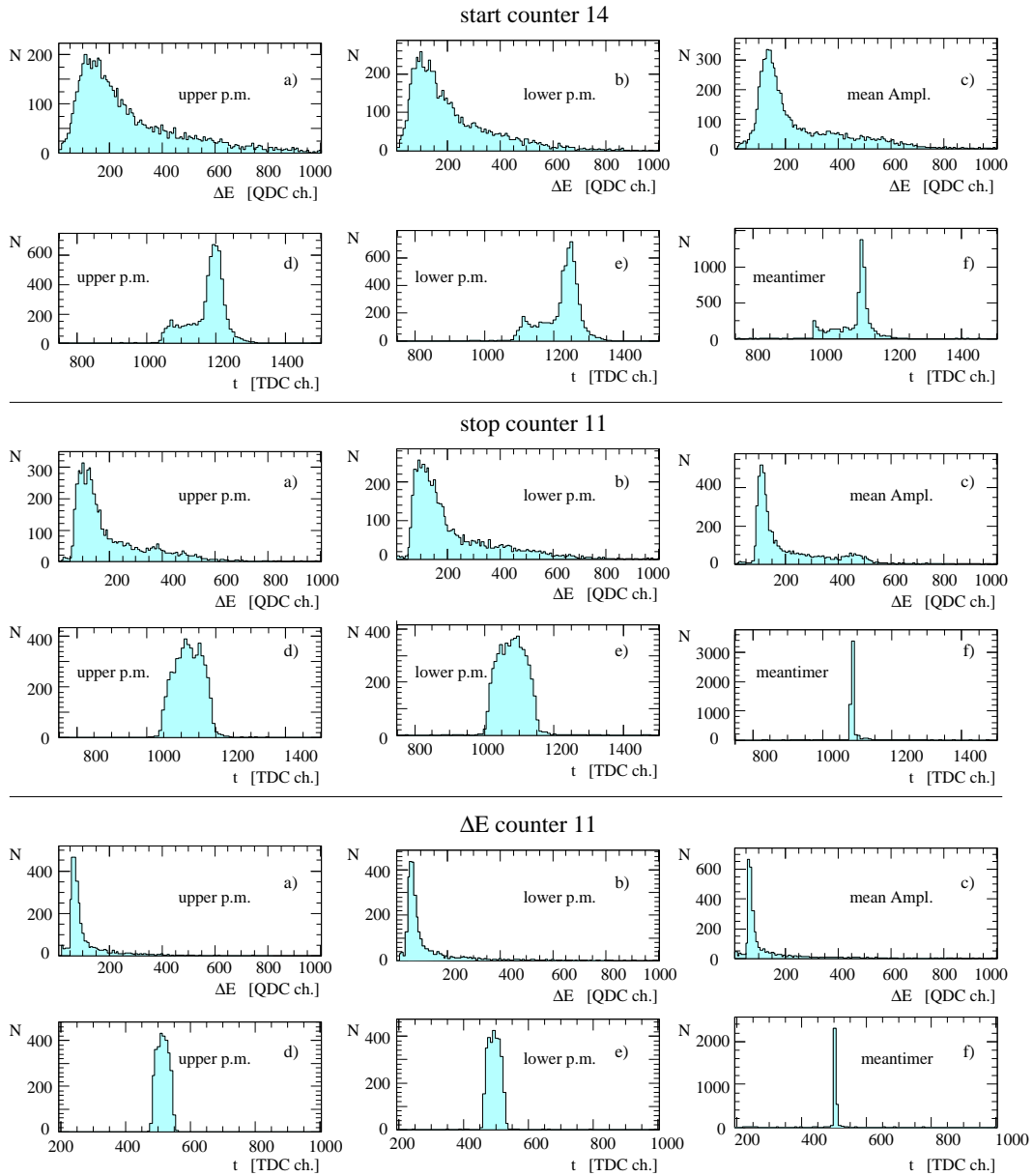


Figure 3.1: For start counter 14, stop and  $\Delta E$  counter 11 the energy loss and the corresponding time–signals from the upper and lower photomultipliers and their mean are shown.

The timing signals depend on the distance of the particle–hit to the upper and lower photomultiplier. Both individual spectra have a width which corresponds directly to the length of the scintillator but the mean value is position–independent. Since the stop counter meantimer starts the time measurements, its meantimer spectrum is a

narrow peak of  $\approx 1$  channel which corresponds to the resolution of the electronics. In all the time spectra the width of a TDC channel is roughly 45 ps. The meantimer-spectrum for the start counters directly represents the time-of-flight spectrum between the start and stop scintillators.

## 3.2 Background Suppression by Tracking

Not all particles which cause a trigger stem directly from the target. Many of the detected particles have been scattered, for example at the pole shoes of D2 (see Fig. 3.2, left side).

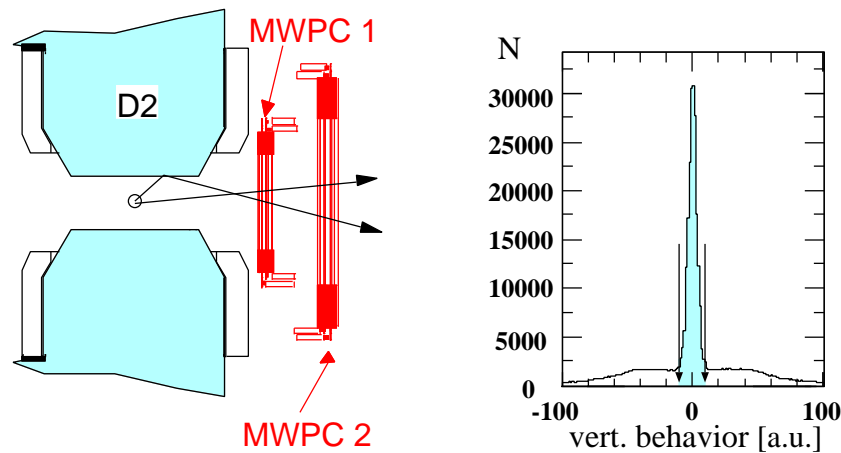


Figure 3.2: Particles scattered at the pole shoes of D2 can be suppressed exploiting their vertical behaviour.

Particles emitted from the target evince a characteristic feature which can be exploited by using the side chambers. When plotting the  $y$ -coordinate of a particle measured in MWPC 1 versus the vertical angle of the particle's track, a straight line is observed from target ejectiles. Scattered particles do not have a correlation between  $y$  and  $\theta$  and therefore can be found anywhere. Such two dimensional spectra are created for each valid start-stop counter combination. The straight line is fitted and all entries are projected perpendicular to the fit-line. Particles ejected from the target lie within a Gaussian shaped peak while the background is uniformly distributed (see Fig. 3.2, right side). Setting a window on the peak (off-line) suppresses most of the scattered background.

Furthermore, accidental coincident particles can be suppressed with the help of the wire chamber information. For a certain start-stop counter combination, particles

can pass only a certain part of the chambers in horizontal direction. Chamber hits which lie outside these so-called corridors are accidental and are rejected in the off-line analysis. The corridors are easily found from experimental data.

### 3.3 Adjustment of the $K^+$ -Selection

The kaon signals cannot be identified without additional criteria. In Fig. 3.3 a the time difference between a hit in stop and veto counter 11 is shown. The peak from the “prompt” pions is seen together with the exponential curve from the  $K^+$  decay products. Requiring a delayed signal in this distribution very efficiently suppresses prompt particles and actively selects kaons. The cut is indicated by the arrow. As an example in Fig. 3.3 b-d the start-stop TOF and the energy loss distributions in the stop and  $\Delta E$  counter are shown for telescope 11 without and with requiring a delayed veto signal. In Fig. 3.3 b an indication on the presence of kaons is seen already without demanding a delayed veto signal. After requiring this signal, pions and protons are strongly suppressed and the kaons are clearly visible. In the energy loss spectra, there is no indication on kaons at all without additional criteria. After demanding a delayed veto signal, the kaon peaks are visible.

In a first round all the data are analysed with this criterion in order to find the kaon peak positions and to set all gates. Subsequently the data are reanalysed without demanding a delayed veto-signal but requiring the unchanged TOF and energy loss gates indicated by the arrows.

### 3.4 Data Preselection

To deal with the huge amount of data, a first (off-line) preselection is performed by rejecting scattered background and accidentals (described above) and requiring the TOF of a kaon (peak position  $\pm 30$  ch.) in order to select particles with the TOF of kaons only. The gates were found with the procedure described above. In Fig. 3.4 the analysis steps are depicted.

Since the TOF resolution is  $\Gamma(\text{FWHM}) \approx 15$  ch. ( $\hat{=} 675$  ps), more than 99% of all kaons are selected. All cuts will be checked later on with clean kaon events and improved statistics. Each run is preselected and stored into a file. The two conditions (chamber information and TOF) are strong criteria and reduce the data files to about 2 GB in total (in compressed format). Those files are the basis for the following analysis steps. All can be analysed together within a few hours. A second preselection is performed by demanding the energy loss of a kaon in the  $\Delta E$  scintillator.

The distributions before and after the preselection are shown in Fig. 3.5. The kaons are clearly observed in the lower figures. A very good identification of kaons is

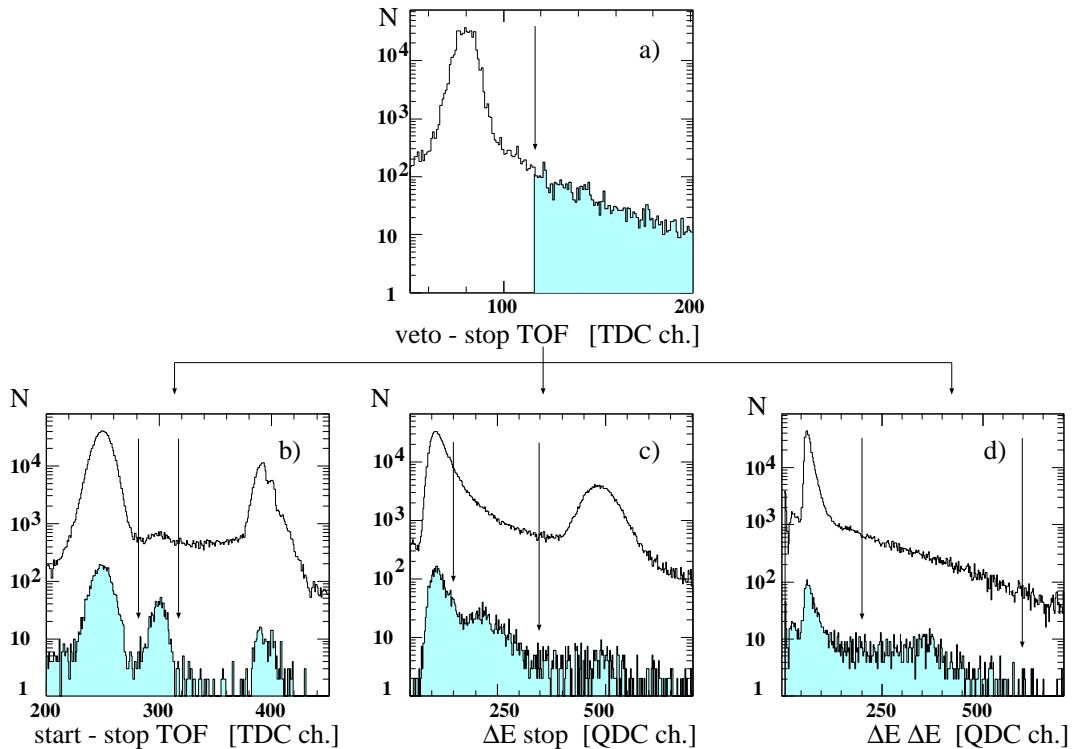


Figure 3.3: In a) the TOF distribution between stop and veto counter 11 is shown. The prompt peak is caused by minimum ionising particles. Requiring a delayed signal (indicated by the arrow), effectively suppresses them whereas kaons survive due to their exponential decline. In b) the TOF distribution between the start counters and stop counter 11 is presented. Without any selection criteria pions, protons and an indication on kaons are seen. With a delayed veto signal, kaons are clearly seen. In c) and d) the energy losses in the stop and  $\Delta E$  scintillator 11 are shown. Without selection criteria the energy losses of pions and protons are observed and no indication on kaons. In events with a delayed veto signal the energy losses of kaons become visible. The arrows in b) and d) indicate the gates used for the preselection of kaons without demanding a delayed veto signal. The chamber information has been exploited for all spectra.

obtained after selecting coincident deuterons in the FDS and is shown later. The gates on TOF and energy loss Fig. 3.5 b-d strongly suppress the prompt particles in the TOF distribution between the veto and stop counter (Fig. 3.5 a). The effectiveness of the individual cuts is demonstrated in Sect. 5.5.

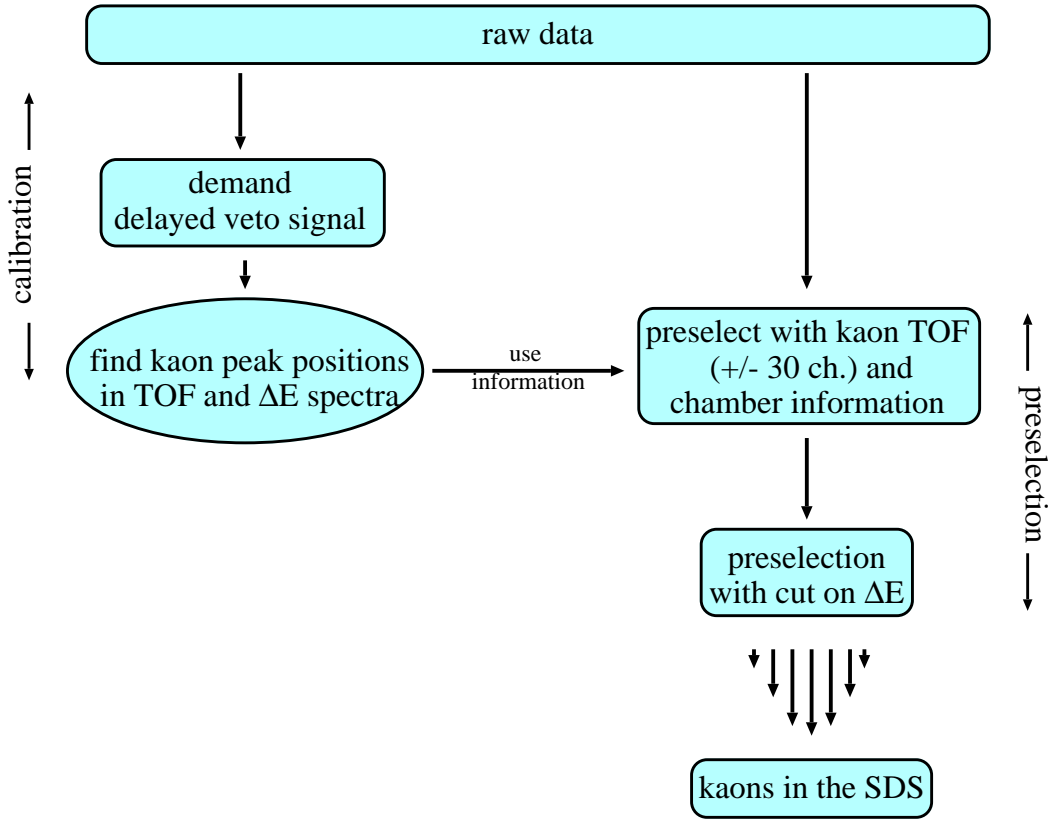


Figure 3.4: Sequence of identifying and selecting kaons in the SDS.

### 3.5 $K^+$ Momentum Reconstruction

The momentum of particles detected in the SDS is reconstructed using a box-field method. In this approach the magnetic field of D2 is approximated by a homogeneous box-field with effective field width and length. The particle's track inside the magnetic field is defined by the Lorentz force which leads to a circular movement. Outside the magnetic field a straight line is assumed. The vertical and horizontal angles derived from the chamber information, are used to calculate the particle's momentum components.

The effective length of the box-field is calculated from the magnetic field strength, the beam momentum and the ANKE deflection angle. The effective width is determined from experimental data using the calibration reaction  $pp \rightarrow pK^+\Lambda(1116)$ . A  $K^+$  meson has been selected in one of the telescopes and a proton in one of the side-wall counters. The kaon and proton momentum components have been determined with the box-field algorithm assuming an estimate for the effective width. Subse-



quently, the missing mass  $m(pp, pK^+)$  was calculated and the effective width tuned such that the  $\Lambda(1116)$  mass was obtained. The achieved momentum resolution for kaons in the momentum range 400 - 625 MeV/c is  $\Delta p/p \sim 2.35\%$  (FWHM).

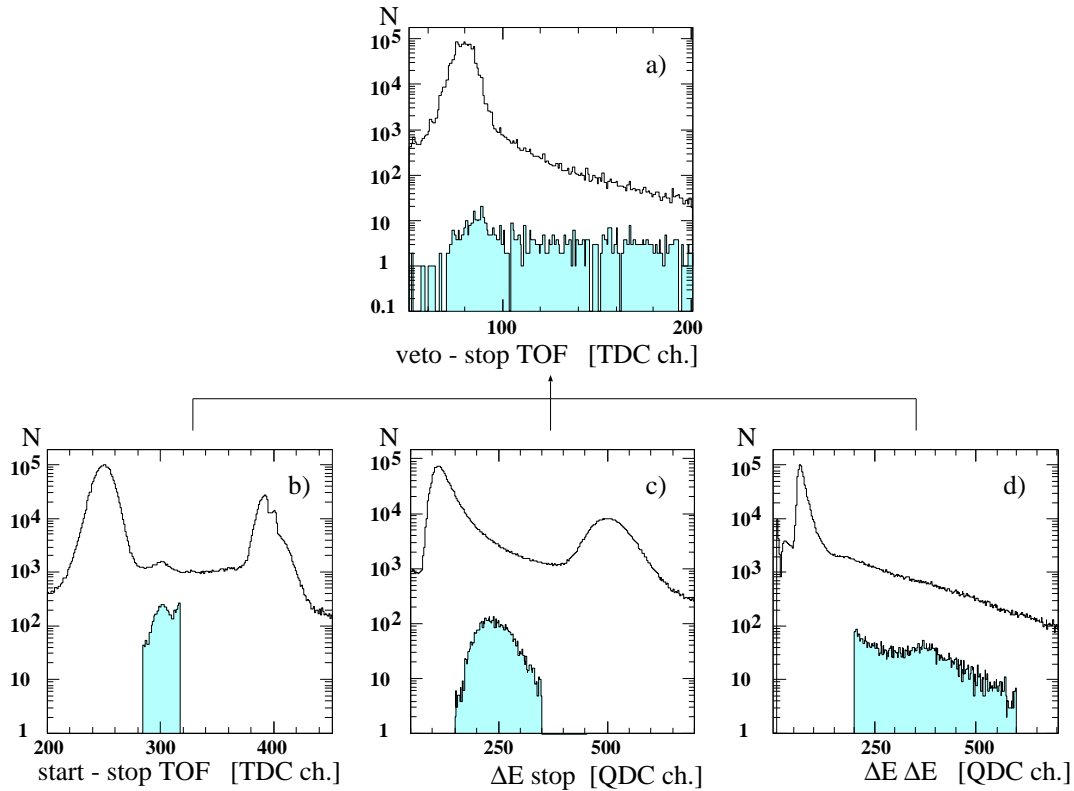


Figure 3.5: The TOF and energy loss distributions before and after setting a gate on the distributions b) - d). In the shaded area of b) the kaon peak is seen on a rising background. In c) a peak structure remains, containing the kaons as well as scattered particles. These particles are mostly protons with about twice the kaon momenta and the same energy loss. Kaons are stopped in the  $\Delta E$  scintillator, resulting in large energy losses. The energy losses of the scattered particles are not characteristic. Thus, a peak on background is observed. The chamber information has been exploited for all spectra.



## 4. Identification of Deuterons

After selecting kaons in the telescopes 10 - 15, coincident protons and deuterons are identified in the FDS by their momentum and relative time to the  $K^+$  mesons. It is shown that protons and deuterons can be well separated.

### 4.1 Momentum Reconstruction in the FDS

For the reconstruction of particle momenta in the FDS a different approach [Vol91] than the boxfield method has been used. The momentum resolution of the boxfield algorithm would be insufficient for the FDS.

In a magnetic field the motion of a particle is determined by the Lorentz force, leading to:

$$m \cdot \frac{d}{dt} \vec{v} = q \cdot \vec{v} \times \vec{B}. \quad (4.1)$$

The solution of this equation depends on five initial parameters  $x_0, y_0, x'_0, y'_0$  and  $\lambda = 1/p$ .  $x_0, y_0$  are the coordinates at some  $z = z_0$ ,  $x'_0, y'_0$  are the derivatives with respect to  $z$ . When assuming a point like target, only  $x'_0, y'_0$  and  $\lambda$  are needed at the target position. The coordinates of the particle are a regular function of the parameters:

$$x_i = x_i(x'_0, y'_0, \lambda) \quad (4.2)$$

$$y_i = y_i(x'_0, y'_0, \lambda) \quad (4.3)$$

Due to the regularity,  $x_i$  and  $y_i$  can be expanded in Taylor series:

$$x_i = \sum_{l,j,k} C_{l,j,k}^x (x'_0)^l (y'_0)^j (\lambda)^k \quad (4.4)$$

$$y_i = \sum_{l,j,k} C_{l,j,k}^y (x'_0)^l (y'_0)^j (\lambda)^k \quad (4.5)$$

The expansion can be restricted to polynomials of a certain degree. It was shown that restricting the sum of  $l, j$  and  $k$  to 4 is sufficient. This implies that 35 coefficients

$C_{l,j,k}^{x/y}$  have to be determined and is done by using a “training sample” which consists of simulated events tracked through ANKE. Subsequently, the coordinates of the particles tracks when crossing the chambers are calculated, and the coefficients are varied such that the difference to the approximated coordinates  $x_i$  and  $y_i$  are minimal. With this method a momentum resolution of typically  $\Delta p/p \sim 2.7\%$  (FWHM) is achieved.

## 4.2 Timing Information

As for the SDS, the similar raw spectra exist for the forward counters. The start signal for the coincidence trigger is a hit in a SDS stop counter. The time distributions of the forward counters relative to such a hit are shown in Fig. 4.1. While the signals from the upper and lower photomultipliers are broad due to different distances to the photomultipliers, the meantimer is narrower and independent of the hit position. The time distributions correspond to the time difference of a particle in the SDS and the FDS. For this figure no preselection was performed. Therefore, the prominent peak is caused by the particles with the highest trigger rates, namely  $\pi^+$ -proton coincidences.

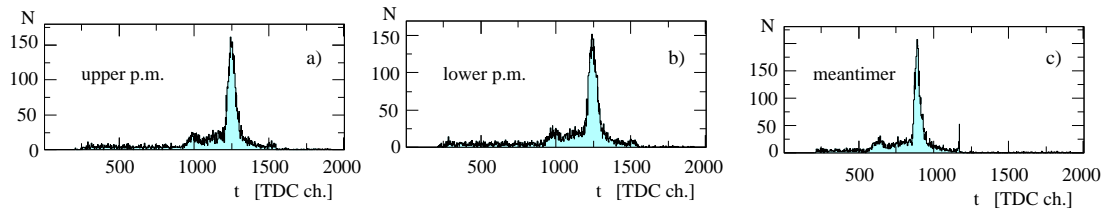


Figure 4.1: The time distributions from forward counter 2 (first layer). Without any preselection mainly  $\pi^+$ -proton coincidences are observed.

A relative calibration of the spectra from the forward counters has been performed using proton-kaon coincidences. For this purpose  $15 \times 17 = 255$  time difference spectra of a particle in the FDS (17 counters) and a second particle in the SDS (15 telescopes) have been created and filled with data when a kaon in the SDS has been selected. (The same procedure was performed for pions.) The time difference spectra for forward counter 2 are shown in Fig. 4.2 a - o for all telescope combinations. (Each forward-telescope combination is summed over the valid start counter combination.) Most of the forward particles are protons. The prominent peak in the time difference spectra is therefore caused by coincident kaon-proton pairs. For each combination

the peak position has been shifted to zero and summed (Fig. 4.2 p):

$$T_{\text{FD}i} = \sum_j (t_{\text{FD}i} - t_{\text{SD-SO}j} - C_{\text{FD}i,\text{SD-SO}j}) \quad (4.6)$$

$T_{\text{FD}i}$  is the time with which spectrum p is filled,  $t_{\text{FD}i}$  is the time from forward counter  $i$  (TDC channel of the meantimer),  $t_{\text{SD-SO}j}$  is the time from stop counter  $j$  and  $C_{\text{FD}i,\text{SD-SO}j}$  is the proton peak position in the difference spectra (a - o). Fig. 4.2 q and r represent the sum over all possible forward-telescope counter combinations of the first and the second layer of the forward hodoscope ( $15 \times 8 = 120$  and  $15 \times 9 = 135$  individual spectra).

$$T_{\text{layer 1}} = \sum_{i=1,8} T_{\text{FD}i}$$

$$T_{\text{layer 2}} = \sum_{i=1,9} T_{\text{FD}i}$$

In each spectrum the peaks have been shifted to zero before summing. In the sum spectra no particles other than protons are seen.

### 4.3 Identification of Protons and Deuterons

For the two hodoscope layers two-dimensional spectra were created where on one axis the time difference of a particle in the FDS and a  $K^+$  in the SDS is plotted while on the other axis the momentum of the forward particle is shown. While in the previous time difference spectra in Fig. 4.2 deuterons cannot be discriminated against protons, in this case two distinct bands are visible; one for protons and one for deuterons. For this figure and in the analysis a gate on energy loss in the forward scintillation counters was set. However, the proton and deuteron energy losses are very similar in this momentum range. The gate mainly helps to reject background events.

In order to select protons or deuterons the corresponding band is fitted by a second order polynomial and each point is projected on the polynomial. The two dimensional figure for layer 1 and the projection on the fit to the proton and deuteron band are shown in Fig. 4.3.

To improve the time resolution the spectra were corrected for the different flight paths, which particles have to cover when for a certain stop counter different start counters were hit. Only events with a hit in forward counter 2 have been selected. For each valid start-stop counter combination, the time difference spectrum to forward counter 2 has been created. Subsequently, the difference to the peak position of the

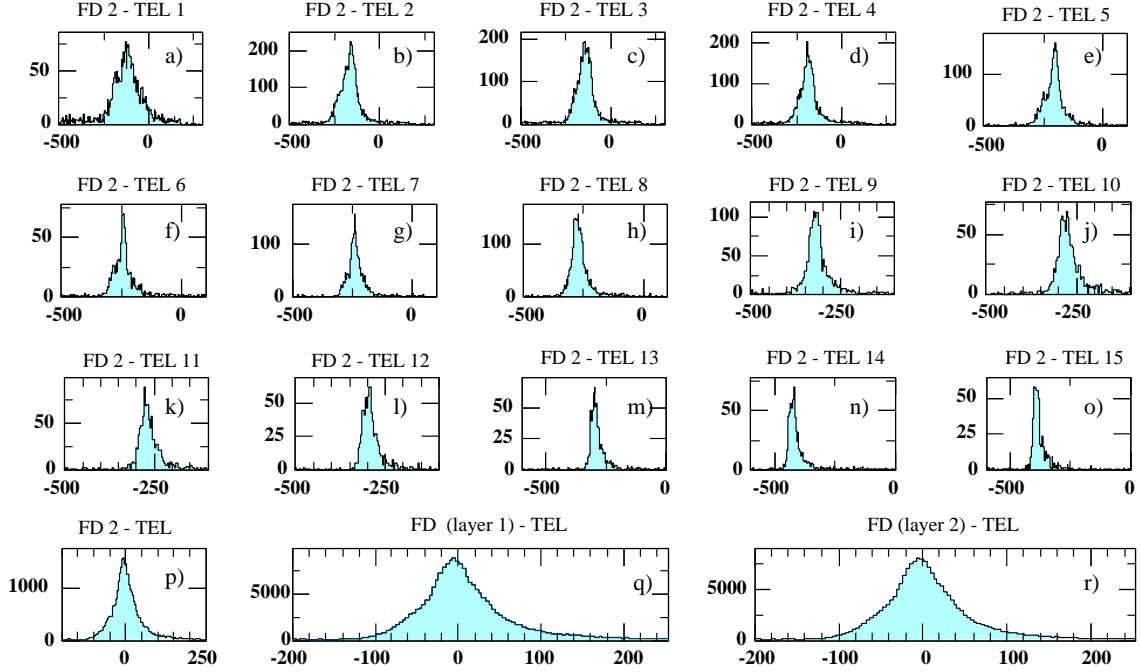


Figure 4.2: The time difference between forward counter 2 and telescopes 1 - 15 (a - o), between forward counter 2 and the sum of these distributions where the peak of each has been shifted to zero (p). In q and r the sum of all possible forward-stop counter TOF distributions for layer 1 and 2 is shown (the peak of each individual distribution shifted to zero).

sum over all combinations (Fig. 4.2 q) has been determined. For this difference has been corrected:

$$T'_{FDi} = \sum_{j,k} (t_{FDi} - t_{SD-SOj} - C_{FDi,SD-SOj} + C_{FD2,SD-SOj} - C_{FDi,SD-SOj,SD-SAk}) \quad (4.7)$$

$T'_{FDi}$  is the corrected time shown in Fig. 4.3 a,  $C_{FD2,SD-SOj}$  is the proton peak position in the time difference spectrum of forward counter 2 and side stop counter  $j$ , while  $C_{FDi,SD-SOj,SD-SAk}$  is the peak position in the time difference spectrum of forward counter  $i$  and side stop counter  $j$  where only stop counter  $k$  has been hit. The procedure is independent of the forward counter since it compensates different flight paths in the SDS only. Counter 2 has been chosen since it is placed near to the beam pipe where the count rate is high. The improvement is shown in Fig. 4.3 b.

The proton and deuteron peak are well separated. Setting a gate on the projected deuteron (proton) peak allows one to identify the reaction  $pp \rightarrow dK^+X$  ( $pK^+X$ ). The corresponding background of protons (deuterons) is negligible. However, there

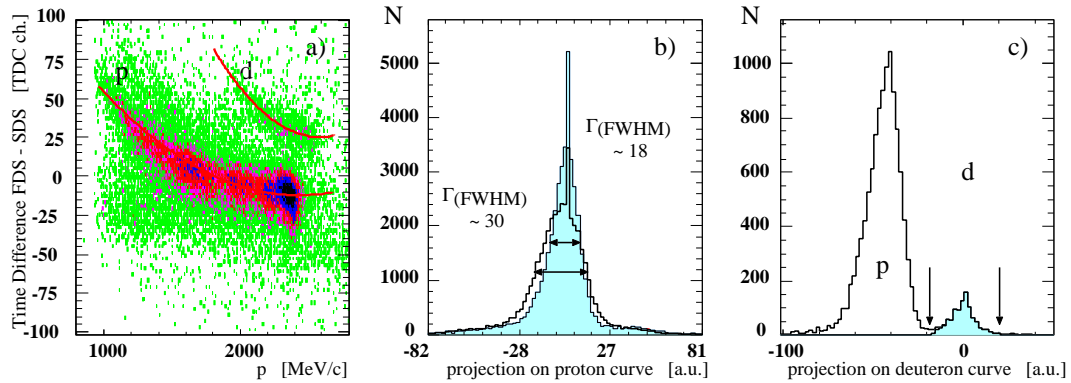


Figure 4.3: In a) the time difference of particles in the FDS and kaons in the SDS (telescopes 10 - 15) versus the momentum of the particles in the FDS. In b) and c) the projection on the proton and deuteron fit curve (solid curves in a) are shown. The broader distribution of b) was obtained before correcting for the different flight paths between the start and stop counter in the SDS. In the narrower distribution the improvement is seen. The units are arbitrary. In c) as shaded distribution the time difference projection is shown for events which survived the selection chain for  $dK^+\bar{K}^0$  events. The unshaded distribution is before a cut on the time difference projection in both layers.

is some flat background of scattered particles which is also visible in the missing mass distribution  $m(pp, dK^+)$ . This will be discussed in the next section.





## 5. Identification of the Reaction

$$pp \rightarrow dK^+ \overline{K}^0$$

After selecting coincident  $pK^+$  and  $dK^+$  pairs, a missing mass analysis is performed. The  $pK^+X$  events are used to confirm the momentum reconstruction and to determine efficiencies. The  $dK^+X$  events are further analyzed and mass and angular distributions are obtained.

### 5.1 Identification of 3-Body-Reactions

For the hypothesis that the coincident  $pK^+$  or  $dK^+$  events are both primarily produced particles of a 3-body reaction, the missing third particle must be a particle with strangeness  $S = -1$ . For coincident  $pK^+$  pairs the missing particle has to be a hyperon and is possibly a  $\Lambda(1116)$ ,  $\Sigma(1193)$ ,  $\Sigma(1385)$  or  $\Lambda(1405)$ . In the second case the missing third particle must be a  $\overline{K}^0$ .

For the momentum reconstruction of particles in the SDS and FDS two different algorithms have been used, the boxfield and polynomial method. To ensure that both algorithms can be used together for coincident side and forward particles,  $pK^+X$  events have been studied. A missing mass analysis reveals the prominent peaks of the light hyperons (see Fig. 5.1). The masses of the  $\Lambda(1116)$  and  $\Sigma(1193)$  hyperons are reproduced within  $\pm 1 \text{ MeV}/c^2$ .

Subsequently, a missing mass analysis of coincident  $dK^+X$  events has been performed. As a result, the missing mass distribution  $m(pp, dK^+)$  is shown in Fig. 5.2 a and b. A peak containing about 1000 events with a width of  $\Gamma = 8 \text{ MeV}/c^2$  is seen at the  $\overline{K}^0$  mass on top of a flat background distribution. Cutting on the peak allows one to select the reaction  $pp \rightarrow dK^+ \overline{K}^0$  with little background due to misidentified particles in the SDS and FDS. Background from other  $dK^+X$  reactions does not exist (strangeness conservation).

In Table 5.1 the number of  $pp \rightarrow dK^+ \overline{K}^0$  events for the different telescopes in which the kaon was identified is listed.

The background below the  $\overline{K}^0$  peak has been estimated by two straight lines (see Fig. 5.2 b), resulting in 110 background events for the upper and 66 events for the

lower line within the accepted mass window. From this a background of  $9.0 \pm 2.3_{\text{sys}}\%$  is derived. The error is the difference to the individual values and considered as the systematic error.

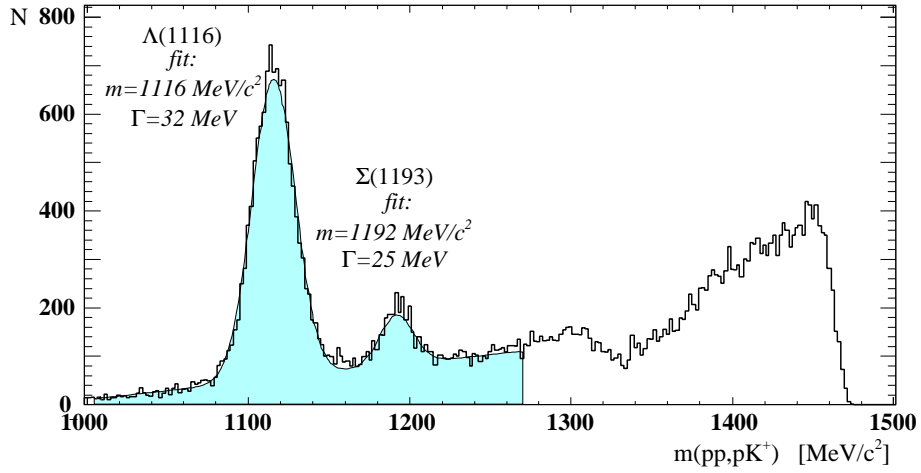


Figure 5.1: Missing mass distribution  $m(pp, pK^+)$ . The  $\Lambda(1116)$  and  $\Sigma(1193)$  masses are reproduced by two Gaussians and a straight line within  $\pm 1 \text{ MeV}/c^2$ .

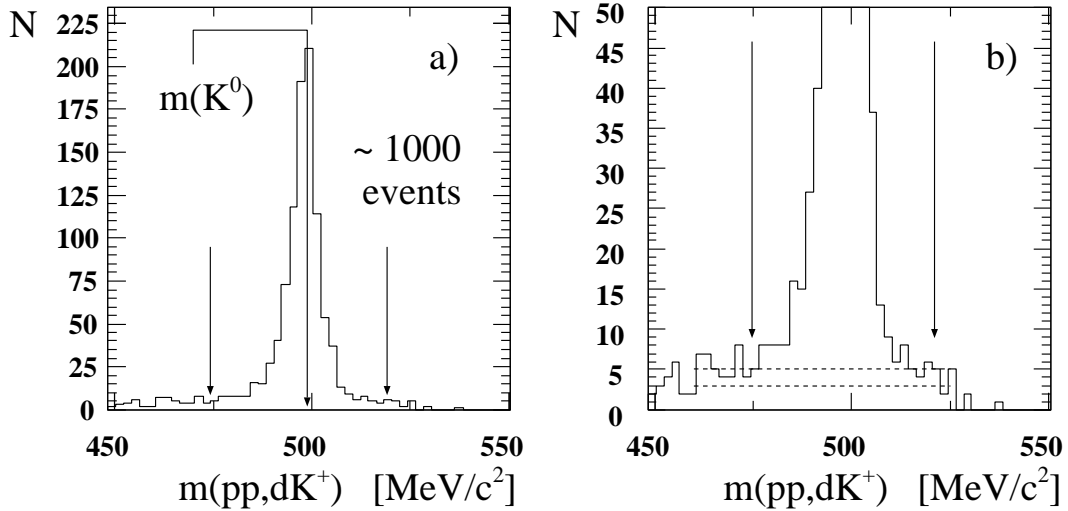


Figure 5.2: Missing mass distribution  $m(pp, dK^+)$ . Within the gates around the  $\overline{K}^0$  peak there are about 1000 events. The fraction of background events was estimated with two different lines in b).

telescope	10	11	12	13	14	15
$N_{tel}$	158	185	219	154	137	122
$\epsilon_{\Delta E}$ [%]	53.0	56.3	49.2	51.7	50.6	49.2
$\epsilon_{SD-MWPC}$ [%]	92.8	91.9	89.3	84.2	80.3	70.8
$\epsilon_{FD-MWPC}$ [%]		←	73	→		

Table 5.1: Identified  $dK^+\overline{K}^0$  events (including  $\sim 9\%$  background) and efficiencies.

## 5.2 Efficiency Determination

All efficiencies have been determined from experimental data. The detection efficiency of the scintillation counters for kaons is close to 100% [Büs02a]. The MWPCs and the cut on energy loss have lower efficiencies which are discussed below.

### 5.2.1 Cut on Energy Loss in the $\Delta E$ counters

The efficiency of the cut on energy loss of kaons in the  $\Delta E$  counters has been determined using the reaction  $pp \rightarrow pK^+\Lambda$ . Selecting kaons by TOF only, demanding coincident protons, performing a missing mass analysis  $m(pp, pK^+)$  and cutting on the prominent  $\Lambda$  peak (Fig. 5.1), leads to relatively clean kaon signals (see Fig. 5.3 a). In order to determine the number of kaons obtained with (Fig. 5.3 b) and without cut on energy loss, the TOF spectra have been fitted with a Gaussian for the kaons and a straight line for the background events. The ratio of events in the Gaussian peaks corresponds to the cut efficiency. This value does not only include the probability that the kaon energy loss lies within the gates but also the probability that a kaon which caused a trigger in the stop counter, reaches the  $\Delta E$  counter. The efficiency has been determined for telescopes 10 to 15 (see Table 5.1) and is shown in Fig. 5.3 a with statistical errors. The values have been fitted with a straight line, resulting in an average efficiency of  $\bar{\epsilon} = 0.515 \pm 0.015$ .

### 5.2.2 Side Chambers

The efficiency of the side chambers has been investigated with particles with the TOF ( $\pm 20$  ch.) and energy loss of a kaon. For each telescope the ratio of events with and without demanding a reconstructed track has been determined, defining the chamber efficiency (see Fig. 5.4 and Table 5.1). A track is reconstructed if a hit in at least two out of three planes per chamber was registered.

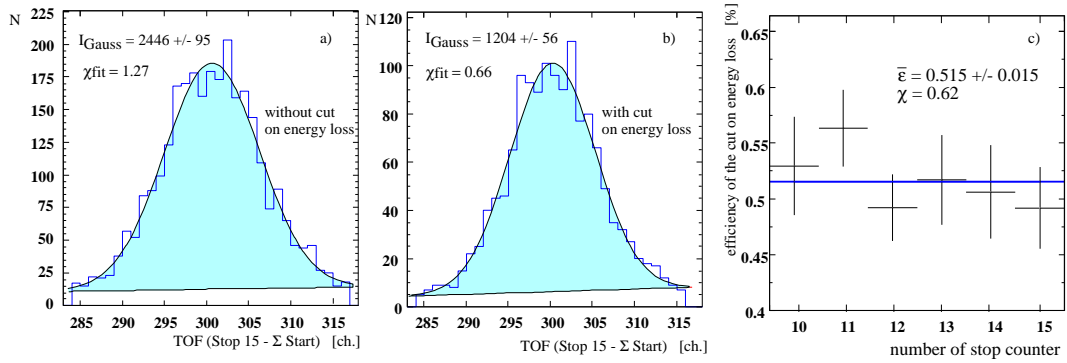


Figure 5.3: TOF distribution between the start counters and stop counter 15 without (a) and with (b) cut on energy loss in the  $\Delta E$  counter.  $pK^+\Lambda$  events where a kaon has been detected in telescopes 10 - 15 and a proton in the FDS have been analyzed. In c) the efficiency of the cut is shown for each telescope. The efficiency has been approximated by a constant.

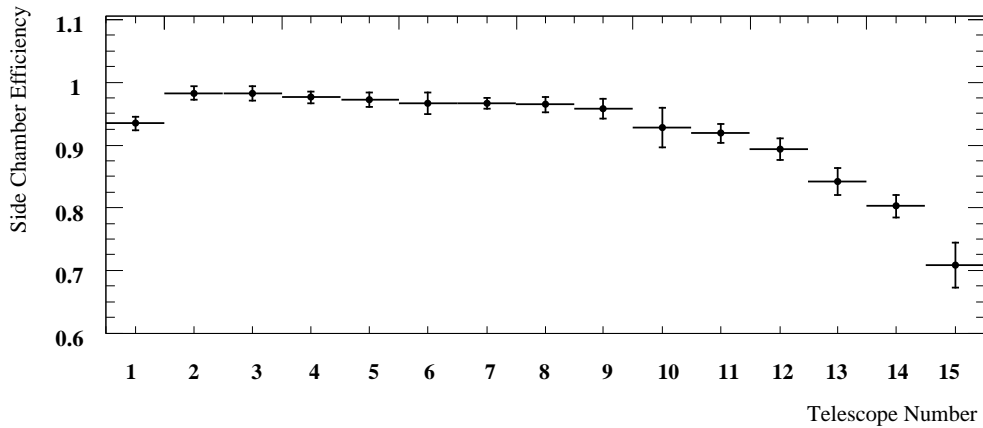


Figure 5.4: Efficiency of the SDS MWPCs for each telescope.

The efficiency was determined for several arbitrarily chosen runs between runs 3276 and 3369. Since the efficiency differs only little from run to run (with few exceptions) it has been averaged. The error obtained is the mean difference to the deduced mean.

### 5.2.3 Forward Chambers

The determination of the forward chamber efficiency is more difficult. In the case of the side chambers a subsequent hit in a start–stop combination ensures that the

particle passed the chambers.

The efficiency value one obtains when selecting a kaon in the SDS and a coincident hit in the hodoscope with and without demanding a reconstructed forward track is about 29%. It is not, however, guaranteed that the forward particle really passed through the chambers.

In order to determine the correct values, a different approach was chosen using the method which has been described in detail in Ref. [Dym01]. Each sensitive plane (X1-3, Y1-3) has been subdivided into  $20 \times 20$  cells. Two planes in X (in Y) were used to reconstruct a track and its crossing with the third plane was calculated. If, for this event, there was a hit in the cell then the cell was assumed to be efficient. Any data sample can be used to determine such efficiency maps for each plane. In order to provide sufficient statistics, data were parasitically recorded with an FD trigger (prescaled by a factor of 999). Average efficiency maps for the runs 3276 - 3369 have been created [Fed02]. Later in the analysis the efficiency of each forward track is calculated event-by-event according to these efficiency maps. The average efficiency to reconstruct a track is 73%.

### 5.3 Effectiveness of the Selection Criteria

In Fig. 5.5 the effectiveness of the applied cuts is demonstrated for the case of the arbitrarily chosen run 3313. The TOF distribution between the start and stop scintillators is plotted for different cut conditions. The solid black distribution (I) represents the raw TOF distribution without any cuts. The prominent pion peak is seen as well as the peak of protons. As described before, most of the events with a proton in the SDS were not recorded since the trigger gates were too narrow. When demanding a track in the SDS, most of the scattered particles are rejected in the analysis (II). An indication for the presence of kaons around channel 300 can already be observed. Cutting mildly on the energy loss of kaons in the stop counters helps to further suppress scattered background (III). A very effective criterion for kaon identification is to cut on the energy loss in the  $\Delta E$  scintillators (IV). With this criterion a clear peak due to kaons is visible and most of the protons and many pions are suppressed. Furthermore, requiring a coincident particle with a reconstructed track mainly decreases statistics due to the efficiency of the forward chambers (V). Asking for a coincident deuteron and a missing  $\bar{K}^0$  leads to a clean kaon peak with little background (shaded distribution). This peak contains the full statistics of the experiment (scaled by 0.2), not only of run 3313.

In order to demonstrate the effectiveness of demanding a delayed veto signal, the experimental TOF distribution is shown with the cuts on the side chambers, the energy loss in the stop scintillators and a delayed veto signal (VI). Clear signal from kaons are observed and these can be separated from pions by cutting on the TOF peak.

This distribution should be compared to distribution III (same conditions but no delayed veto signal is demanded). The cut on a delayed veto signal is very effective but has a low efficiency. It has not been used since the number of  $dK^+\bar{K}^0$  events is limited and we have shown that kaons can be clearly identified without asking for a delayed veto signal (shaded distribution).

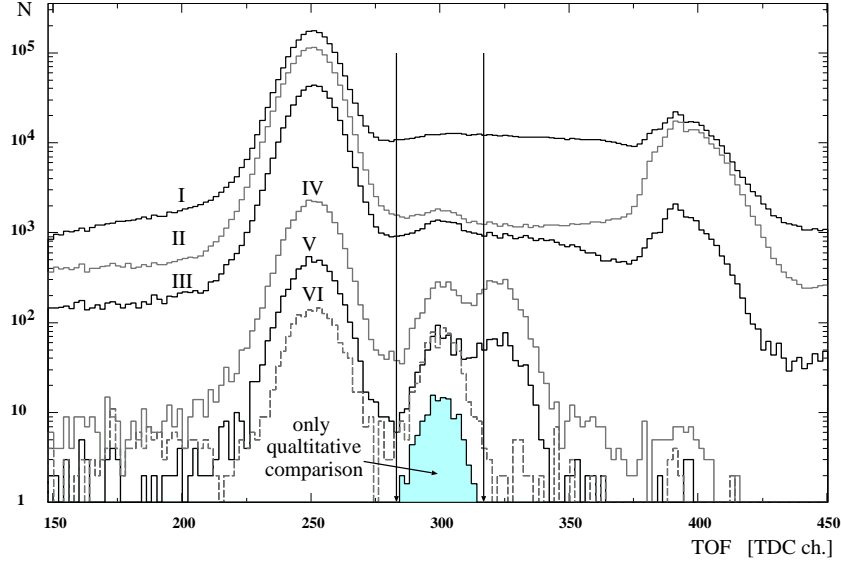


Figure 5.5: Effectiveness of different cuts demonstrated on the TOF distribution between all valid start and stop counters in the SDS (run 3313). The distributions are without any selection criteria (I), with suppression of background exploiting the chamber information (II), with an additional gate on the energy loss in the stop counters (III), with furthermore requiring the energy loss of a kaon in the  $\Delta E$  counters (IV) and plus a reconstructed track in the FDS (V). Curve VI represents the TOF distribution after background suppression by the side chambers, a cut on energy loss in the stop counters and a delayed signal in the veto counters (c.f. curve III). The shaded distribution is the TOF of the  $K^+$  mesons from all identified events of the whole beamtime with a coincident deuteron and a missing  $\bar{K}^0$  is shown as a qualitative comparison.

## 5.4 Analysis of $dK^+\bar{K}^0$ Events

One of the analysis goals is to investigate mass and angular distributions. The missing mass  $m(pp, d)$  has been calculated (see shaded distribution of Fig. 5.7 a). A narrow distribution at the mass of the  $a_0$  is observed. It is limited by the  $K\bar{K}$  threshold at low masses and by the maximal accessible mass for  $T_p = 2.65$  GeV at high masses. A second mass has been analyzed,  $m(pp, K^+)$ , and is presented in

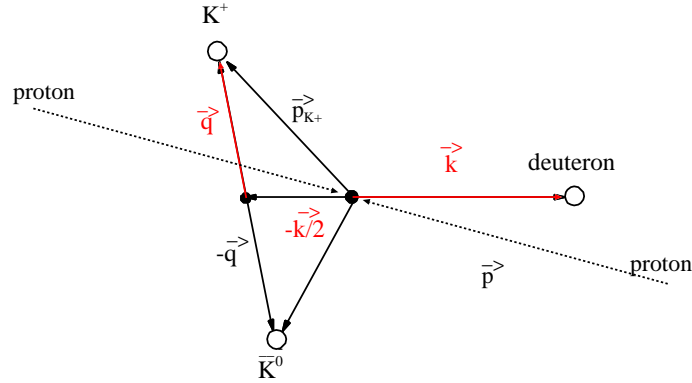


Figure 5.6: Momentum vectors in the center-of-mass. The vectors  $\vec{k}$  and  $\vec{q}$  define the reaction plane which does not necessarily contain  $\vec{p}$ .

Fig. 5.7 b. It evinces a strong rise which is dominated by the ANKE acceptance (as shown later).

The  $dK^+\bar{K}^0$  system in the  $pp$  center-of-mass (cms) can be described according to Fig. 5.6. The deuteron momentum is labeled by the vector  $\vec{k}$ , the relative momentum of the two kaons by  $\vec{q}$  and the proton beam by  $\vec{p}$ . The kaon momentum vector  $\vec{p}_{K^+}$  is equal to  $\vec{q} - \vec{k}/2$ . In an unpolarized measurement the angular distributions relative to the beam have to be symmetric to  $\cos\alpha = 0$  (or  $\alpha = 90^\circ$ ).

As explained in Sect. 7.3, the final state interactions (FSI) influence the distributions at these angles. The experimental distributions are shown in Fig. 5.7 c - e (shaded). They are additionally presented after correcting for the chamber efficiency. The efficiency of the side chambers is taken into account as a function of the hit telescope whereas the forward chamber efficiency is calculated for each track from the efficiency maps. The average corrections factor is  $\epsilon = 0.624$ . In order to simplify the comparison of the uncorrected and corrected distributions, the corrected distributions have been scaled by 0.624.

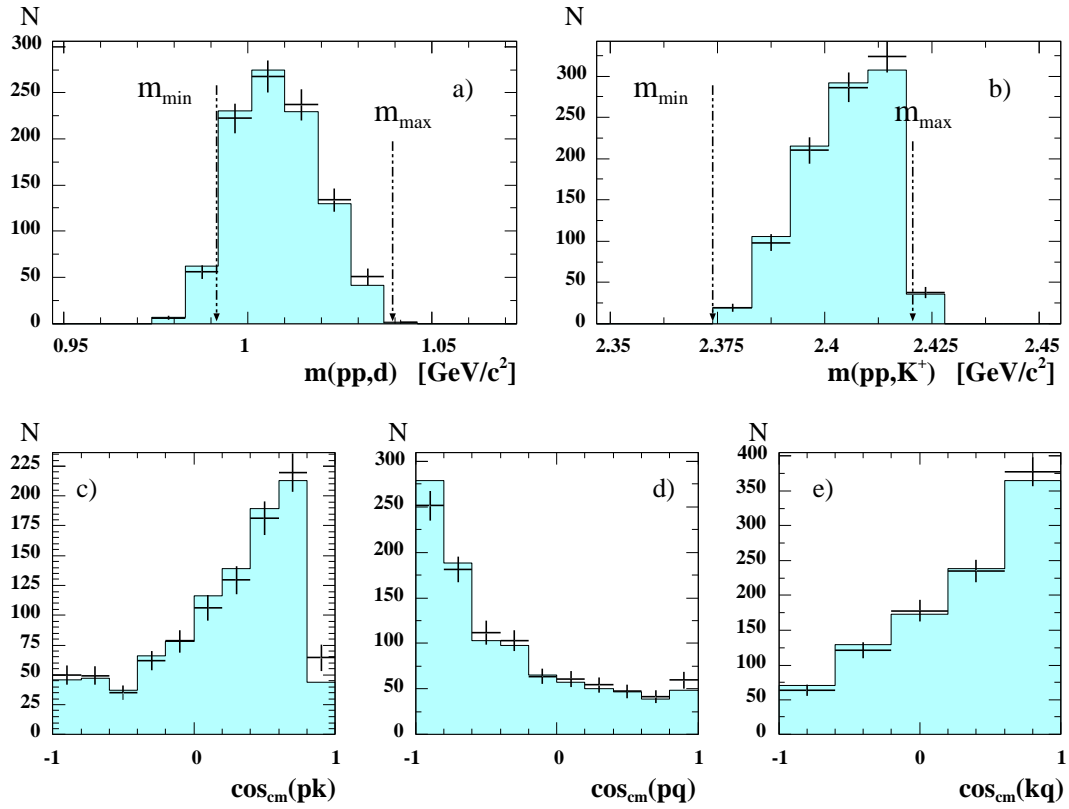


Figure 5.7: Experimental distributions without (shaded) and with chamber efficiency correction (bars). In order to simplify the comparison of the uncorrected and corrected distributions, the corrected distributions have been scaled by the average (SDS and FDS) chamber efficiency of  $\epsilon = 0.624$ .



## 6. Simulations on the Reaction

$$pp \rightarrow dK^+\overline{K}^0$$

In order to determine the total cross section  $\sigma_{\text{tot}}(pp \rightarrow dK^+\overline{K}^0)$  as well as differential distributions ( $d\sigma/dm, d\sigma/d\Omega$ ) from the spectra shown in Fig. 5.7, the total geometrical acceptance of ANKE and the acceptance as a function of kinematic variables has been studied with the help of Monte-Carlo simulations. In Sect. 6.1, the total acceptance is determined for different initial distributions at the target in order to obtain an estimate for the systematic uncertainties. In Sect. 6.2, the procedure of the differential acceptance correction is outlined.

### 6.1 Total Acceptance

To illustrate the acceptance of ANKE for coincident  $dK^+\overline{K}^0$  events produced in  $pp$  collisions at  $T_p=2.65$  GeV, the horizontal and vertical momentum ( $p_x$  and  $p_y$ ) of deuterons and kaons is shown in Fig. 6.1 versus their longitudinal momentum  $p_z$ . The closed curves define the kinematic limits. Low momentum kaons are detected in telescopes 10 - 15, and deuterons with (mostly) negative horizontal momentum  $p_x$  in the FDS. In the vertical direction the gap height of D2 limits the acceptance. In order to correct the measured distributions for the limited acceptance of ANKE depicted in Fig. 6.1, simulation calculations have been performed. The program GEANT 3 has been used in which the ANKE detectors have been implemented (ANKE-GEANT, [Zyc02]).

Different distributions have been generated and were tracked in ANKE-GEANT. In order to compare them with experimental data, the same conditions were applied, e.g. only valid start-stop counter combinations, a hit in telescopes 10 - 15, a coincident hit in the first and the second FDS hodoscope layer and passing through the chambers. Small angle scattering, energy losses and decay in flight were included in the simulations.

The total acceptance  $\alpha$  is defined as the ratio of  $pp \rightarrow dK^+\overline{K}^0$  events surviving the selection chain to the amount of started events. Since the initial distribution at the target is unknown at this stage of the analysis, different target distributions were

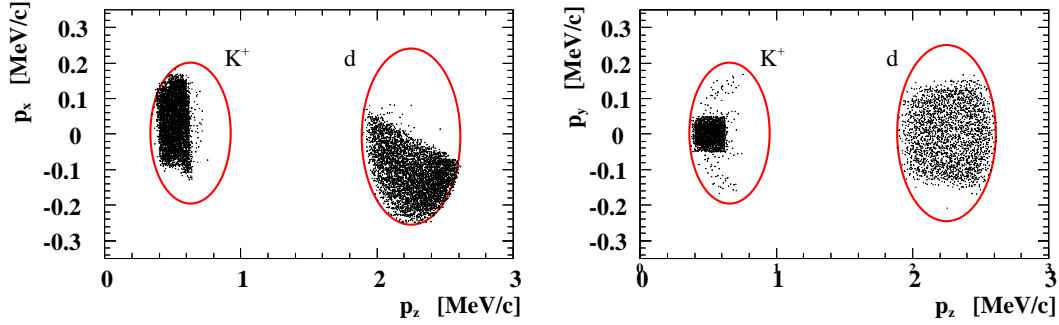


Figure 6.1: Horizontal and vertical momentum of kaons and deuterons versus their longitudinal momentum, reflecting the acceptance of ANKE for coincident  $dK^+\overline{K}^0$  events. The closed curve is the kinematic limit for  $T_p=2.65$  GeV.

considered. The first distribution was phase space, which is physically it not allowed since there are only  $S$ -waves involved (see Sec. 1.3). For a phase-space distribution the cosines of the angles between the proton beam and the deuteron  $\hat{p} \cdot \hat{k}$ , the beam and the relative kaon momentum  $\hat{p} \cdot \hat{q}$  and the deuteron and the relative kaon momentum  $\hat{k} \cdot \hat{q}$  are uniformly distributed (the notation  $\hat{\phantom{x}}$  symbolizes unit vectors). Subsequently, the angles  $\hat{p} \cdot \hat{k}$ ,  $\hat{p} \cdot \hat{q}$  and  $\hat{k} \cdot \hat{q}$  have been modified separately and the influence on the total acceptance was studied for each angle (see Table 6.1). In addition, the model distribution from Ref. [Bra02] has been used. The total acceptances as determined in these simulations are listed in Table 6.1.

They vary between 1.13 and 2.96%, depending on the choice of the initial distribution. For distribution VI from Table 6.1, which is closest to the experimental one, a total acceptance of  $\alpha = (2.20 \pm 0.05_{\text{stat}})\%$  has been obtained. For the determination of the total cross section (see Sect. 7.1) a value of  $\alpha = (2.20 \pm 0.20_{\text{sys}})\%$  is used. The larger systematic error allows for (unknown) uncertainties of the acceptance-correction procedure from Sec. 6.2 and would include the cases of phase-space production or distributions according to the model from Ref. [Bra02] or some of the cases I-V in Table 6.1.

## 6.2 Differential Acceptance Correction

In order to correct differential distributions, e.g. angular and missing mass distributions, in a model independent way, a different approach was chosen. It is necessary to determine the dependence of the acceptance on a set of kinematic variables that fully describes the reaction. For a three body reaction, the number of degrees of freedom is 5. In a first approach two invariant squared masses,  $m^2(K^+\overline{K}^0)$  and  $m^2(d\overline{K}^0)$ , and three Euler angles have been chosen. The Euler angles describe the

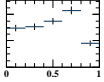
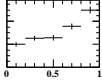
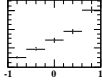
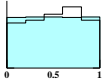
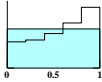
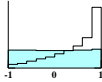
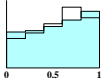
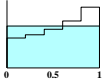
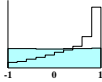
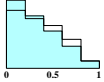
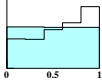
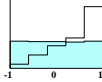
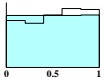
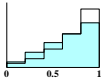
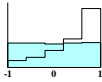
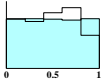
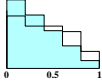
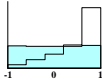
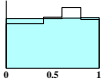
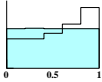
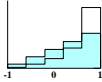
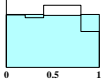
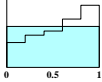
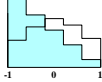
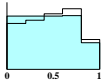
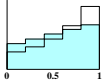
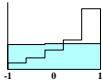
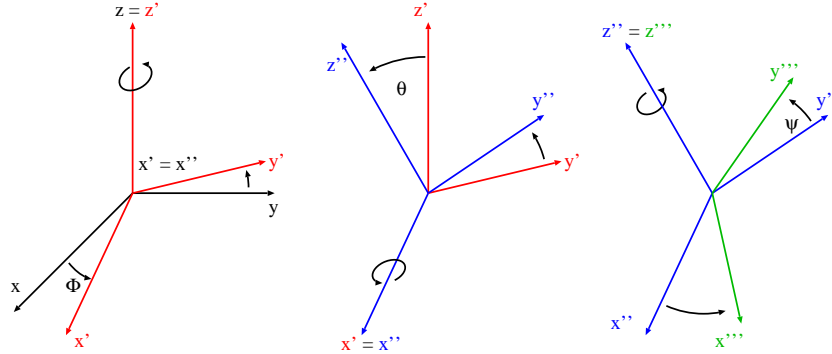
distribution	$ \cos(pk) $	$ \cos(pq) $	$\cos(kq)$	acceptance
exp.				
phase space				$(2.05 \pm 0.04_{stat})\%$
model [Bra02]				$(2.21 \pm 0.05_{stat})\%$
I				$(2.09 \pm 0.04_{stat})\%$
II				$(2.40 \pm 0.05_{stat})\%$
III				$(1.66 \pm 0.04_{stat})\%$
IV				$(2.96 \pm 0.05_{stat})\%$
V				$(1.13 \pm 0.03_{stat})\%$
VI				$(2.20 \pm 0.05_{stat})\%$

Table 6.1: Total acceptance for different initial distributions. The shaded distributions are the initial distributions at the target while the unshaded distributions are observed at ANKE. The number of started events is the same for all simulated distributions. In the first row the experimental distributions are shown (see Sect. 5.4). Distributions I - VI are different from a phase space distribution only in the indicated angle.

matrix element	$m1$	$m2$	$m3$	$m4$
variable	$m^2(K^+\bar{K}^0)$	$m^2(d\bar{K}^0)$	$ \cos(\theta_{cm}(d)) $	$\psi_{cm}(K\bar{K})$
number of bins	5	5	5	4
variable	$ \cos_{cm}(pk) $	$ \cos_{cm}(pq) $	$\cos_{cm}(kq)$	$E_{cm}(d)$
number of bins	5	5	5	4

Table 6.2: Definition of the acceptance matrices I and II.

orientation of the reaction plane,  $\theta_{cm}(d)$ ,  $\phi_{cm}(d)$  and  $\psi_{cm}(K\bar{K})$  (see Fig. 6.2). In an unpolarized measurement the cross section does not depend on the azimuthal angle of the deuteron  $\phi_{cm}(d)$  and isotropic behavior in this distribution was assumed. The other four variables have been subdivided into bins which were used to define an acceptance matrix. The variables and number of bins are listed in the upper part of Table 6.2. Since there are two identical particles in the initial state,  $\theta_{cm}(d)$  has to be symmetric around  $90^\circ$  and only absolute values of  $\cos \theta$  have been studied. In the Euler angle picture the polar deuteron angle  $\theta_{cm}(d)$  corresponds to  $\hat{p} \cdot \hat{k}$  and  $\psi_{cm}(K\bar{K})$  is equivalent to the triple scalar product of the deuteron, proton beam and  $K^+$  vectors,  $(\hat{k} \times \hat{p}) \cdot \hat{p}_{K^+}$ .

Figure 6.2: Definition of the Euler angles  $\theta_{cm}$ ,  $\phi_{cm}$  and  $\psi_{cm}$ . The z-axis is along the beam direction.

In a second approach, four different variables have been used, namely  $\hat{p} \cdot \hat{k}$ ,  $\hat{p} \cdot \hat{q}$ ,  $\hat{k} \cdot \hat{q}$  and  $E_{cm}(d)$ .  $\hat{p} \cdot \hat{k}$  and  $\hat{p} \cdot \hat{q}$  have to be symmetric and only the absolute values have been studied (lower part of Table 6.2).

In total for each matrix there are  $5 \times 5 \times 5 \times 4 = 500$  elements. 90 million phase-space events have been generated and tracked through ANKE-GEANT. A transversal tar-

get extension of Gaussian shape with  $\Gamma = 5\text{mm}$  has been assumed, multiple angle scattering, energy losses and decay in flight have been taken into account.

The distribution  $N(m)$  over the matrix elements of matrix I and II of particles at the target has been determined. It is presented in the upper row of Fig. 6.3 in a linear scale from which the index of the matrix element can be calculated according to

$$m = (m1 - 1) * 100 + (m2 - 1) * 20 + (m3 - 1) * 4 + m4 . \quad (6.1)$$

The same procedure was used for particles which survived the selection chain. The acceptance is determined by dividing  $N(m_{at\ ANKE})$  and  $N(m_{at\ target})$  and is shown in the lower row of Fig. 6.3.

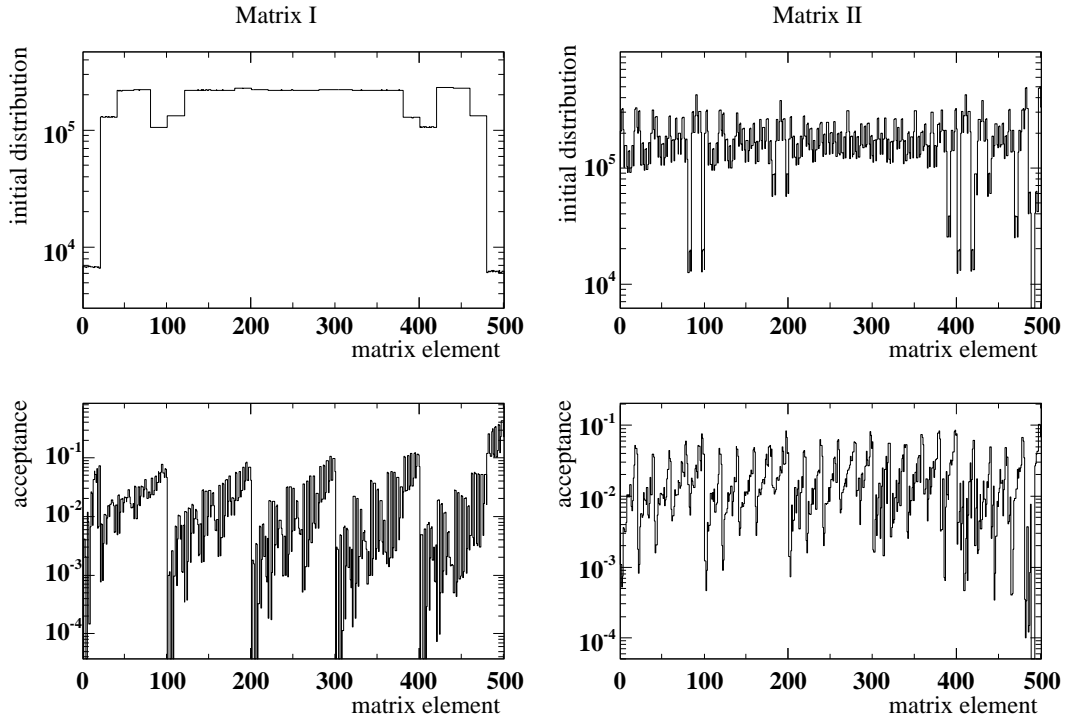


Figure 6.3: Initial distribution over the matrix elements I and II and acceptance in linear presentation.

In principle this method of acceptance correction is model independent. The binning of the variables could give rise to systematic errors when reconstructing distributions different from a phase space distribution. In order to check this assumption, different initial distributions have been tracked through ANKE-GEANT and the simulated distributions observed at ANKE have been corrected for acceptance.

In the first and second row of Fig. 6.4 the deuteron missing mass  $m(pp, d)$  and kaon missing mass  $m(pp, K^+)$  are shown for phase space and the model distribu-

tion [Bra02]. The solid lines are the initial distributions, the dashed what is observed at ANKE. On the latter the acceptance correction has been performed using matrix I. The points with error bars represent the result. The error bars are only statistical. In case of the phase-space distribution the deviations from the initial distribution arise from the few acceptance holes in matrix I (see Fig. 6.3). It turned out that for the correction of a particular distribution more reliable results are obtained if this kinematic variable is explicitly included in the matrix. Therefore, the masses are corrected using matrix I.

For the reconstruction of the angles  $\hat{p} \cdot \hat{k}$ ,  $\hat{p} \cdot \hat{q}$  and  $\hat{k} \cdot \hat{q}$ , matrix II was used. The comparison has been done for all initial distributions indicated in Table 6.1. In Fig. 6.4 examples for a phase-space distribution and those which significantly differ from phase space are shown. The distributions not displayed can be reconstructed equally well.

In contrast to the experimental data, simulated distributions are in principle not limited in statistics. To estimate the uncertainty of the acceptance correction imposed on a sample of about 1000 events, 100 sets of simulated events, each containing 1000 events, have been acceptance corrected and the standard deviation of the mean value for each distribution has been calculated binwise. For this purpose a distribution has been used which is similar to the acceptance-corrected experimental distribution (see Table 6.1, IV, and Fig. 7.3). The result is presented in Fig. 6.5. The error bars are the standard deviation of the mean. They have been added quadratically to the statistical error of the experimental acceptance corrected data. It is slightly bigger than the statistical error. The average deviations of  $\Delta N$  from zero in Fig. 6.5 reflect the systematic error of the acceptance-correction procedure for a distribution similar to the experimental result and is shown in Fig. 7.3 by the shaded areas.

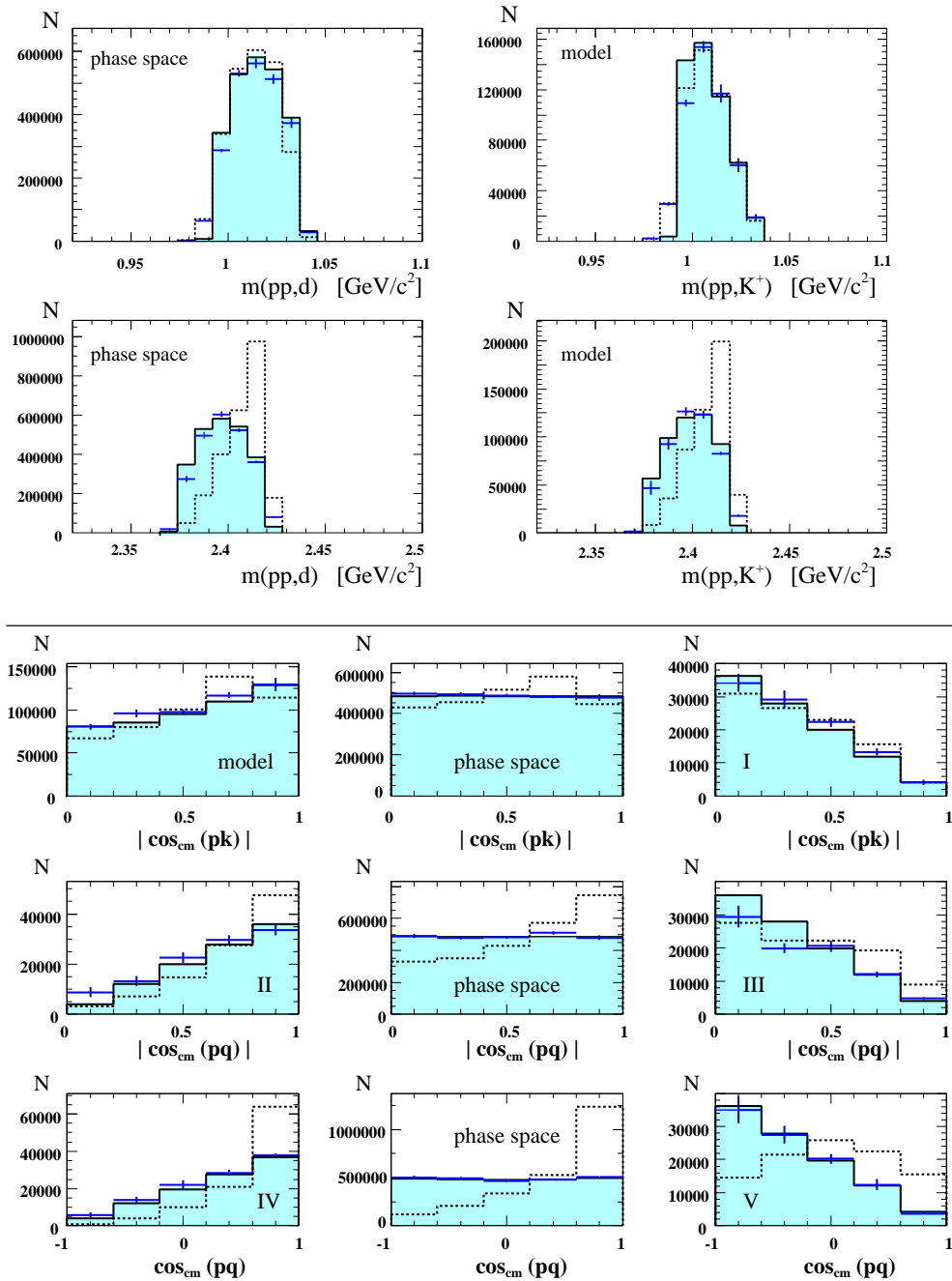


Figure 6.4: Acceptance correction of different distributions. The solid lines represent the distributions started the target, the dashed lines show the distributions observed at ANKE (normalized to the number of started events). The latter distributions have been acceptance corrected, resulting in the distribution symbolized by the points with (statistical) error bars (no normalization!). The mass distributions were corrected with matrix I, the angular distributions with matrix II.

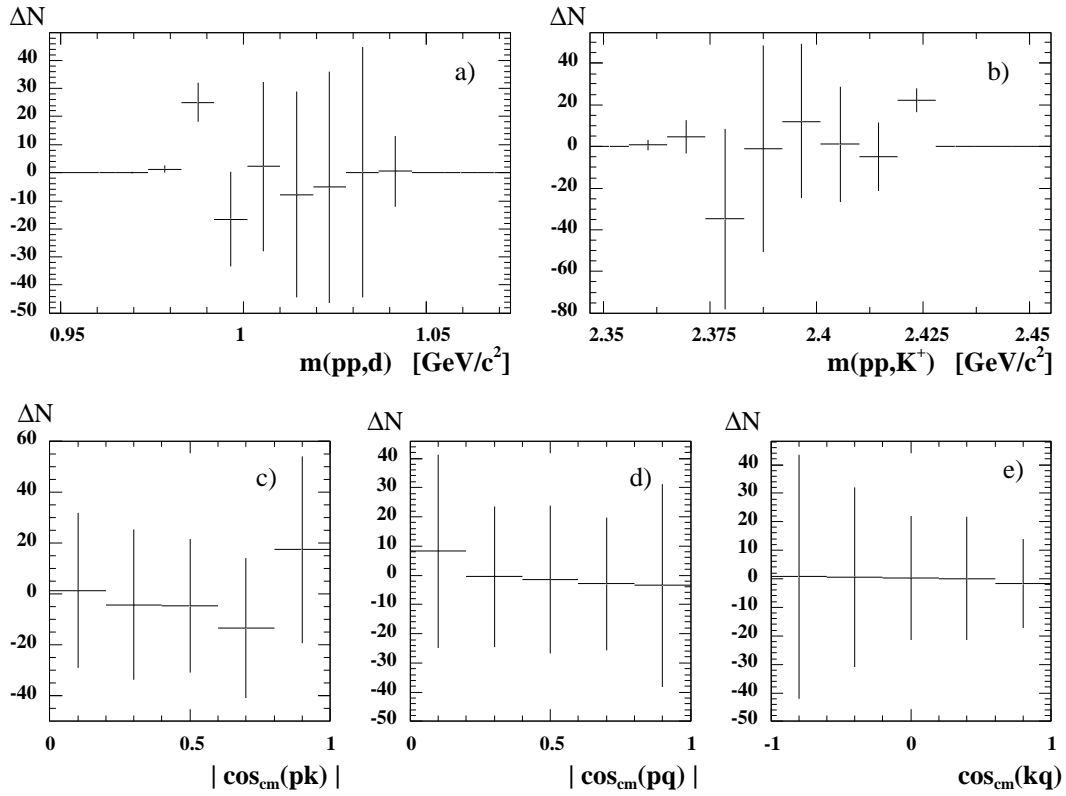


Figure 6.5: Statistical and systematic errors of the acceptance correction for a distribution similar to the experimental results (see Fig. 7.3). 100 sets of 1000 events distributed as in Table 6.1 VI have been corrected for acceptance and the deviation to the initial distribution has been determined binwise.



# 7. Results and Interpretation

## 7.1 Total Production Cross Section

The total production cross section of the reaction  $pp \rightarrow dK^+\overline{K}^0$  has been determined according to the expression:

$$\sigma_{\text{tot}} = \frac{\sum_{\text{tel}=10}^{\text{tel}=15} \frac{N_{\text{tel}}}{\epsilon_{\text{SD-MWPC}}}}{t_{\text{eff}} \cdot L_{\text{av}} \cdot \alpha \cdot \epsilon_{\Delta E} \cdot \epsilon_{\text{FD-MWPC}}} \quad (7.1)$$

$N_{\text{tel}}$  : number of  $dK^+\overline{K}^0$  events after background subtraction  
with a  $K^+$  identified in telescope number “*tel*”, see Table 5.1

$\epsilon_{\text{SD-MWPC}}$  : corresponding side chamber efficiency, see Sect. 5.2.2

$t_{\text{eff}}$  : effective time of the data-taking corrected for the  
deadtime of the DAQ, see Table A.1

$L_{\text{av}}$  : average luminosity during the measurement,  
 $L = (2.70 \pm 0.1 \pm 0.7) \cdot 10^{31} \text{ s}^{-1} \text{ cm}^{-2}$ , see Ref. [Fed01]

$\alpha$  : total geometrical acceptance, see Sect. 6.1

$\epsilon_{\Delta E}$  : average efficiency of the cut on  $K^+$  energy loss  
in the telescopes, see Sect. 5.2.1

$\epsilon_{\text{FD-MWPC}}$  : average efficiency of the forward chambers, see Sect. 5.2.3

The measurement time and deadtime of the DAQ are listed in Table A.1 of the Appendix. The luminosity has been determined using elastically scattered protons where the cross section is known. These events are parasitically recorded with trigger *T2*. The procedure of luminosity determination has been described in Ref. [Fed01]. The systematic error is dominated by the uncertainty in the total cross section for elastic proton-proton scattering.

All other quantities in Eq. 7.1 have been derived before. According to this equation the total production cross section for the reaction  $pp \rightarrow dK^+\bar{K}^0$  is:

$$\sigma = (38 \pm 2_{\text{stat}} \pm 14_{\text{sys}}) \text{ nb.}$$

In Ref. [Gri02] a prediction for the total cross section is given as a function of the excess energy  $Q$ . Some parameters of this model have been fixed to describe the differential cross section for the reaction  $pp \rightarrow da_0^+$  at  $p_p = 3.8, 4.5$  and  $6.3 \text{ GeV}/c^2$  [Abo70]. The prediction for the total cross section is shown in Fig. 7.1, where the solid curve represents the cross section of the reaction  $pp \rightarrow da_0^+(980) \rightarrow dK^+\bar{K}^0$  while the dashed curve symbolizes non-resonant  $K^+\bar{K}^0$  production. The prediction for the total cross section is in very good agreement with the experimental value. According to the model, about 70% of the  $K^+\bar{K}^0$  pairs detected at ANKE stem from an  $a_0^+$  decay, while the rest is produced non-resonantly.

For illustration two other data points are shown in Fig. 7.1 for the reaction  $pp \rightarrow ppK^+K^-$ . The COSY-11 [Que01] data point has been measured at an excess energy of  $Q=17 \text{ MeV}$  and the DISTO [Bal01] data point at  $110 \text{ MeV}$ .

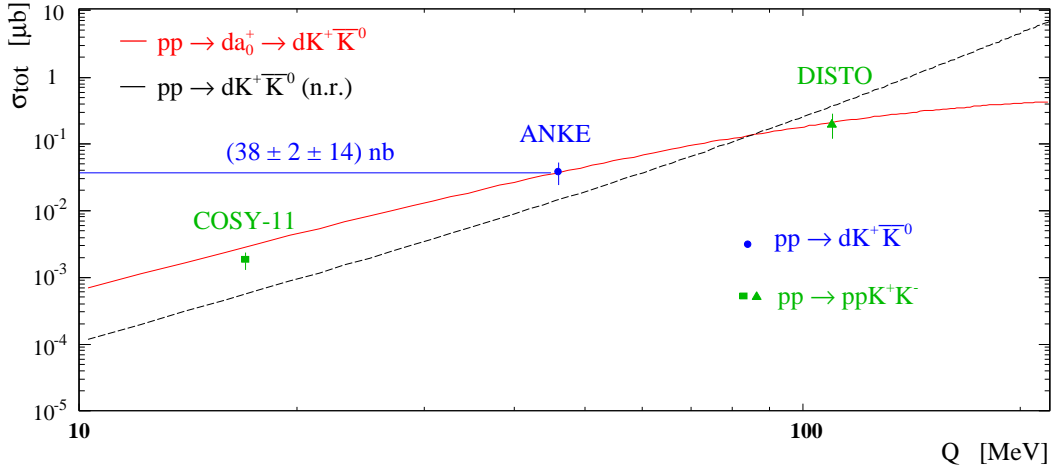


Figure 7.1: Total production cross sections as a function of excess energy  $Q$ . The solid curve is the prediction for the reaction  $pp \rightarrow da_0^+(980) \rightarrow dK^+\bar{K}^0$  whereas the dashed curve represents the non-resonant reaction  $pp \rightarrow dK^+\bar{K}^0$  [Gri02]. The ANKE-data point is shown with statistical and systematic errors. The COSY-11 [Que01] and DISTO [Bal01] data points represent the total cross sections for the reaction  $pp \rightarrow ppK^+K^-$ .

## 7.2 Mass Distributions

The two missing mass distributions  $m_{\text{miss}}(pp, d)$  and  $m_{\text{miss}}(pp, K^+)$  have been corrected for acceptance according to the procedure from Sect. 6.2 and are shown in Fig. 7.2. The error bars are statistical errors. The shaded bars indicate the systematic error caused by the acceptance correction. The total acceptance can be determined from this distribution as well. The result is  $\sigma = 36 \text{ nb}$  and thus consistent with the value from above.

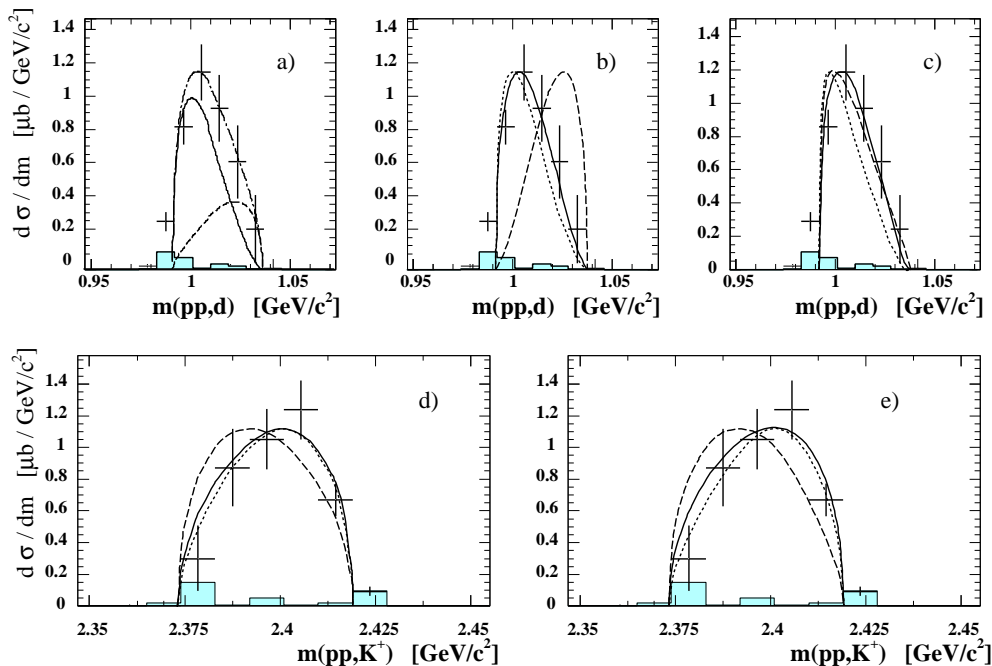


Figure 7.2: Acceptance corrected missing mass distributions  $m(pp, d)$  and  $m(pp, K^+)$ . The experimental data are shown with statistical error bars. The shaded areas indicate the systematic error. The curves are described in the text.

The deuteron missing mass  $m_{\text{miss}}(pp, d)$  (upper figures) is equivalent to the invariant mass of the  $K\bar{K}$  system and reflects the FSI between the two kaons. The predicted invariant mass distribution of Ref. [Gri02] for  $K\bar{K}$  production via the  $a_0$  is shown as the solid curve in Fig. 7.2 a whereas the non-resonant (dominated by  $K\bar{K}$   $P$ -waves) contribution is shown as dashed curve. The dashed-dotted curve is the sum of both and is in good agreement with the data (normalized to the data).

The solid and dotted curves in Fig. 7.2 b are calculated within a simple phase space approach [Cer02] and show the mass distribution with  $S$ -wave production in the kaon system and a  $p$ -wave for the deuteron. The solid curve corresponds to non-resonant  $K\bar{K}$ -pair and the dotted curve to resonant production via the  $a_0$  (c.f. Fig. 1.3). The

dashed curve represents non-resonant  $K\bar{K}$  production with a  $P$ -wave between the kaons. The aim of this approach is not to predict the cross section but to describe the shape of the experimental distribution. The curves are scaled such that the maxima have the same value as the highest data point. Our data seem to favour an  $S$ -wave between the two kaons which is in agreement with the prediction from Ref. [Gri02]. It is generally believed that  $S$ -wave  $K\bar{K}$ -pairs with small relative energies (which is the case close to the  $K\bar{K}$  threshold) undergo a strong FSI via the  $a_0$  resonance.

In Ref. [Ose01] it has been suggested that the reaction  $pp \rightarrow dK^+\bar{K}^0$  is sensitive to both the meson-meson and meson-deuteron FSI, the latter driven by the  $\Lambda(1405)$ . As solid curve in Fig. 7.2 c the distribution is shown if no FSI would contribute. The dotted (dashed) curve represents the distribution with a certain set of parameter for meson-meson (and meson-deuteron FSI). It is interesting to note that within the approach of Ref. [Ose01] the shape of the  $K\bar{K}$ -mass distribution is not well described taking into account the meson-meson FSI only. A better agreement is achieved when the meson-deuteron FSI is included. Also here, a qualitative description of the mass distribution is given and the distributions are scaled to the highest experimental data point. However, the model of Ref. [Ose01] contains free parameters that are to be fixed to our data. Thus, the dotted and dashed curves represent one possible solution only. The distributions with and without FSI are very similar. At this beam energy, the  $K^+\bar{K}^0$  invariant mass is not sensitive to the FSI. However, in the data from the measurement at higher energy the mass interval is substantially wider and the influence of FSI will be studied there.

The kaon missing mass  $m_{\text{miss}}(pp, K^+)$  or invariant mass of the deuteron-antikaon system  $m_{\text{inv}}(d\bar{K}^0)$  is mainly influenced by the deuteron-antikaon FSI, mediated e.g. by the  $\Lambda(1405)$  resonance in the  $n\bar{K}^0$  system. In Fig. 7.2 e the corresponding distributions of Ref. [Ose01] are compared to the data with and without FSI (dotted/dashed and solid curves, resp.). There seems to be a slight discrepancy between the data and the full FSI solution. However, this could also be attributed to the parameter set which has not yet been adjusted. In Fig. 7.2 d, the distributions of Ref. [Cer02] are shown. The dashed curve corresponds to the distribution with a  $P$ -wave in the kaon system (c.f. dashed curve in Fig. 7.2 b) while the solid and dotted curve represent a  $S$ -wave distribution in the kaon system for non-resonant and resonant  $K\bar{K}$  production (c.f. solid and dotted curve in Fig. 7.2 b). As for the  $K\bar{K}$  invariant mass, the data seem to favor the latter, i.e.  $S$ -wave in the kaon system and  $P$ -wave between the deuteron and the kaon system.

### 7.3 Angular Distributions

In order to study the partial wave decompositions in more detail, three angular distributions have been determined and are shown in Fig. 7.3. These are the angles

between the beam and the deuteron  $\hat{p} \cdot \hat{k}$ , between the beam and the relative kaon momentum  $\hat{p} \cdot \hat{q}$  and between the deuteron and the relative kaon momentum  $\hat{k} \cdot \hat{q}$ . The total cross sections obtained from the angular distributions is  $\sigma = 38$  nb. Based on the assumption that only the lowest partial waves contribute, i.e.  $S$ - and  $P$ -waves, the angular distributions can be described model independently ([Han02], see App. A.2). Two FSIs can influence the angular distributions, the FSI in the  $K\bar{K}$  system and in the  $d\bar{K}$  system (see Fig. 7.3 a) The  $a_0$  will enhance the  $Sp$  state where the kaons have small relative momenta (notation see Sect.1.3).

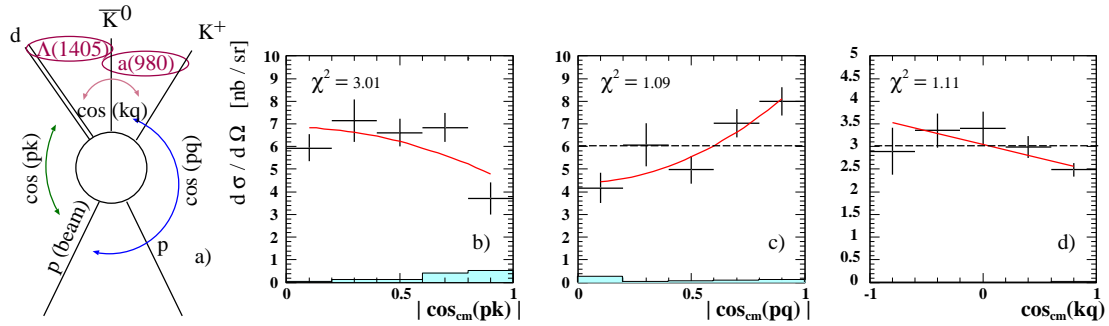


Figure 7.3: a) Notation of the momenta and angular distributions. In the ingoing channel are the two protons (beam momentum  $\vec{p}$ ), in the exit channel the deuteron ( $\vec{k}$ ),  $K^+$  and  $\bar{K}^0$  (relative momentum  $\vec{q}$ ). Acceptance corrected angular distributions are shown in b) - d) with statistical (error bars) and systematic error (shaded bars). The fit was performed with first and second order polynomials (see App. 7.2) whereas the straight line indicates the expectations in c) and d) if all  $K^+\bar{K}^0$  pairs were  $a_0^+$  decay products (no  $d\bar{K}$  FSI).

Following Ref. [Han02], the angular distributions can be described by up to second order polynomials:

$$\begin{aligned} \frac{d\sigma}{d(\cos_{\text{cm}}(pk))} &\propto C_0 + \frac{1}{3}C_{pq2} + C_{pk2} \cdot (\cos_{\text{cm}}(pk))^2 \\ \frac{d\sigma}{d(\cos_{\text{cm}}(pq))} &\propto C_0 + \frac{1}{3}C_{pk2} + C_{pq2} \cdot (\cos_{\text{cm}}(pq))^2 \\ \frac{d\sigma}{d(\cos_{\text{cm}}(kq))} &\propto C_0 + \frac{1}{3}(C_{pq2} + C_{pk2}) + (C_{qk} + \frac{1}{3}C_{pkpq}) \cdot (\cos_{\text{cm}}(kq)). \end{aligned} \quad (7.2)$$

The corresponding fits with their  $\chi^2$  values per degree of freedom are shown in Fig. 7.3 and the extracted coefficients are listed in Table 7.1.

If the observed  $dK^+\bar{K}^0$  events would be produced via the reaction  $pp \rightarrow da_0^+$  only, the angular distributions between the proton beam and the relative kaon momentum  $\cos_{\text{cm}}(pq)$  and between the deuteron and the relative kaon momentum  $\cos_{\text{cm}}(kq)$

parameter	$C_0$	$C_{pk2}$	$C_{pq2}$	$C_{qk} + \frac{1}{3}C_{pkpq}$
fit result	5.28	-2.54	4.57	-0.60

Table 7.1: Result of fitting the experimental distributions.

would be flat (indicated by the dashed curves). Thus, we see from the angular distributions that there has to be some contribution from  $K\bar{K}$   $P$ -waves (see Fig. 7.3 a). However, due to the presence of spins, the argument cannot be reversed: a flat angular distribution does not imply pure  $S$ -wave dominance since several  $P$ -waves can interfere destructively (see App. A.2). The distributions  $|\cos_{\text{cm}}(pq)|$  and  $\cos_{\text{cm}}(kq)$  are described well by the fit curves. However, the  $\chi^2$  per degree of freedom of the fit to the angular distribution  $|\cos_{\text{cm}}(pk)|$  is  $\sim 3$  and the result strongly depends on the experimental point at forward/backward angles. It is interesting to note that a negative slope of the distribution is obtained if terms contribute significantly where the  $a_0^+$  couples to the spin of the deuteron or to the spin of the initial state. The model of Ref. [Gri00] predicted a positive slope. It might happen that this model underestimates the coupling. However, this conclusion depends on one experimental point only and the results should be confirmed by other measurements, e.g. the ANKE  $a_0^+$  experiment at  $T_p = 2.83$  GeV. Note also that there is an interference between the  $K\bar{K}$   $S$ - and  $P$ -waves (see Fig. 7.3 d).

## 7.4 Conclusions

The measured total cross section  $\sigma_{\text{tot}}(pp \rightarrow dK^+\bar{K}^0) = (38 \pm 2_{\text{stat}} \pm 14_{\text{sys}})$  nb is very close to the value predicted by Ref. [Gri02]. Within this model resonant  $a_0^+$  production dominates as compared to nonresonant  $K^+\bar{K}^0$  production. This conclusion is also suggested by the comparison of the mass distribution  $m_{\text{inv}}(K^+\bar{K}^0)$  with the model. In Ref. [Ose01] it has been suggested that also the  $d\bar{K}$  FSI could contribute. From the angular distributions it can be ruled out that the events are produced only via  $a_0$  production which would imply flat angular distributions  $|\cos_{\text{cm}}(pq)|$  and  $\cos_{\text{cm}}(kq)$ . It is not possible to derive the share of the two competing FSI ( $K\bar{K}$ ,  $d\bar{K}$ ). However, the angular distributions indicate that there is a contribution from  $K\bar{K}$   $P$ -wave and interference of  $K\bar{K}$   $S$ - and  $P$ -waves.

## 8. Outlook

The measurement described in this thesis is the first in a series to study the light scalar resonances  $a_0(980)/f_0(980)$  in  $pp$ ,  $pn$ ,  $pd$  and  $dd$  reactions with ANKE ([Cer97], [Büs01]). In this measurement not only coincident  $dK^+$  (discussed here) but  $d\pi^+$  events have also been investigated. For these  $d\pi^+$  pairs an  $\eta$  peak is observed in the missing mass  $m(pp, d\pi^+)$  sitting on top of a broad background from multiple pion production. In the corresponding missing mass  $m(pp, d)$  a shoulder at the mass of the  $a_0(980)$  is seen. After background subtraction based on the assumption of equal background behavior around the  $\eta$  peak, a peak structure is revealed which is shown in Fig. 8.1 b. The analysis of this reaction channel is still in progress and is the topic of a different PhD thesis [Fed02].

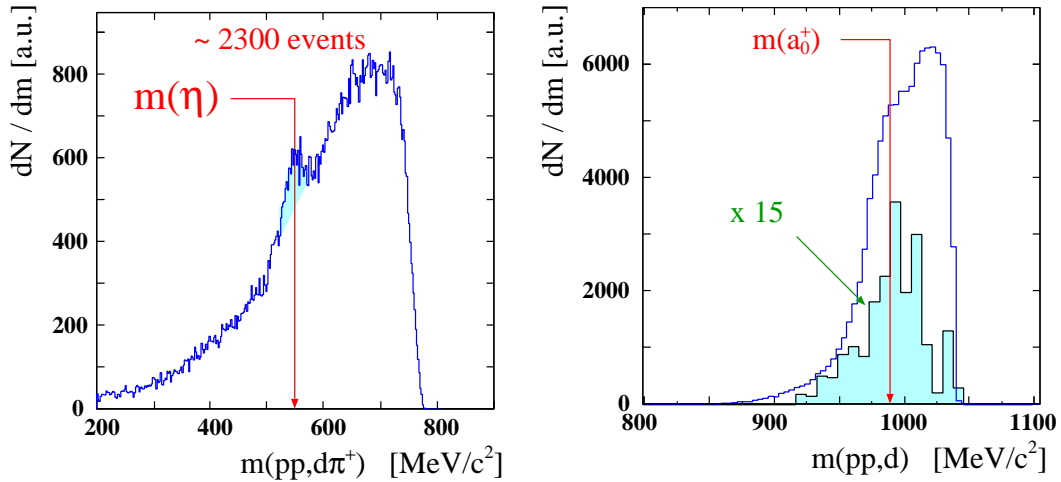


Figure 8.1: Preliminary missing mass distributions of coincident  $d\pi^+$  pairs at  $T_p = 2.65$  GeV.

The combined results from the analysis of both reactions  $pp \rightarrow dK^+\overline{K}^0$  and  $pp \rightarrow d\pi^+\eta$  will be used to derive an estimate of the branching ratio  $a_0 \rightarrow K^+\overline{K}^0/\pi^+\eta$ . In the beginning of 2002 a second measurement on the reaction  $pp \rightarrow dK^+(\pi^+)X$  has

been performed at  $T_p=2.83$  GeV, after the COSY crew managed to achieve higher proton beam energies than before. In a preliminary analysis the  $\overline{K}^0$  has been observed and the missing mass  $m(pp, d)$  covers a substantially wider mass range (see Fig. 8.2).

From this mass distribution it will be easier to distinguish  $K\overline{K}$  pairs which are produced via the  $a_0$  or nonresonantly. The solid and dotted line represent the mass distributions of Ref. [Gri02] for resonant and nonresonant  $K^+\overline{K}^0$  production in the predicted ratio. The dashed–dotted line is the sum of both distributions. The distributions are scaled to fit the data.

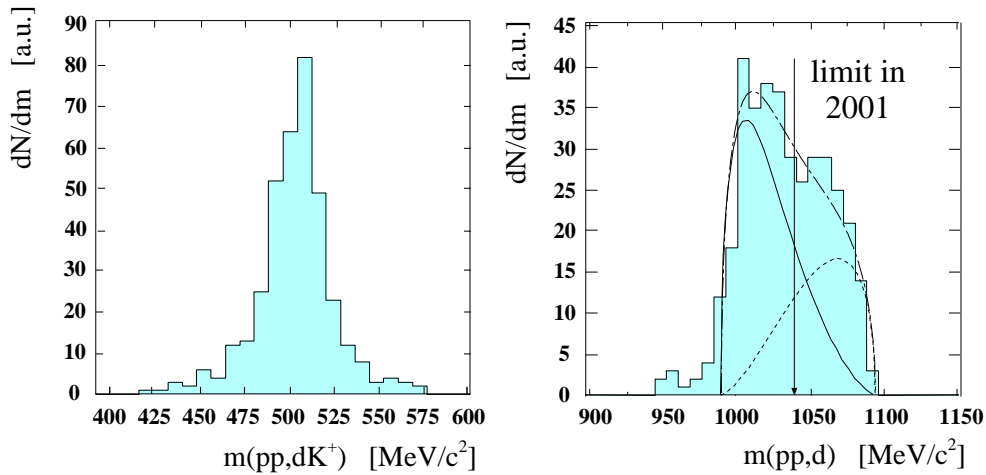


Figure 8.2: Preliminary missing mass distributions of coincident  $dK^+$  pairs at  $T_p = 2.83$  GeV. The solid and dashed lines are the mass distributions of Ref. [Gri02] for resonant and nonresonant  $K^+\overline{K}^0$  production in the predicted ratio. The sum (dashed–dotted line) is normalized to the data and describes them very well. However, the distribution presented here is obtained after a very first analysis without any corrections for efficiency and acceptance, and conclusions cannot be drawn yet.

In the measurement two layers of sidewall counters were used and placed at a distance of about 1 m behind each other, allowing one to set a TOF gate additional to the start–stop gate. In a preliminary analysis, kaons could be observed in the sidewall counters as well. Being able to identify kaons in the telescopes and the sidewall counters increases the statistics and (even more important) the acceptance. A proposal to investigate  $a_0/f_0$  production in  $pn$  and  $pd$  collisions has already been accepted [Büs01] and a proposal for  $dd$  collisions is in preparation. In these reaction channels both the  $a_0$  and  $f_0$  can be produced and mixing effects may distort angular distribution [Büs02b].





# A. Appendix

## A.1 List of Runs

Run	Tape	meas. time	trig_in/ trig_out	effect. time	Trigger $T_1$	Trigger $T_2$	Trigger $T_3$	Events
3277	13	5888	0.316	1861	(T+S)*F	F/999	(T+S)/200	15494764
3278	13	5552	0.316	1755	(T+S)*F	F/999	(T+S)/200	14667137
3279	13	2557	0.314	803	(T+S)*F	F/999	(T+S)/200	6765006
3280	13	4192	0.321	1346	(T+S)*F	F/999	(T+S)/200	11042386
3281	13	5865	0.323	1894	(T+S)*F	F/999	(T+S)/200	15402908
sum		24054		7658				63372201
3290	14	6042	0.323	1952	(T+S)*F	F/999	(T+S)/200	15876848
3291	14	4701	0.258	1213	(T+S)*F	F/999	(T+S)/200	13386507
3292	14	5775	0.277	1600	(T+S)*F	F/999	(T+S)/200	16112748
sum		16518		4764				45376103
3294	15	3796	0.291	1105	(T+S)*F	F/999	(T+S)/200	10413573
3295	15	7347	0.300	2204	(T+S)*F	F/999	(T+S)/200	19765545
3296	15	5354	0.281	1504	(T+S)*F	F/999	(T+S)/200	15102389
3297	15	4202	0.275	1156	(T+S)*F	F/999	(T+S)/200	11936548
sum		20698		5969				57218055
3298	16	414	0.277	115	(T+S)*F	F/999	(T+S)/200	1172234
3299	16	396	0.277	110	(T+S)*F	F/999	(T+S)/200	1132759
3300	16	810	0.280	227	(T+S)*F	F/999	(T+S)/200	2315566
3301	16	3167	0.279	883	(T+S)*F	F/999	(T+S)/200	9011607
3303	16	6541	0.277	1812	(T+S)*F	F/999	(T+S)/200	18450149
sum		11328		3147				32082315
3309	17	7681	0.270	2074	(T+S)*F	F/999	(T+S)/200	20429434
3310	17	4954	0.288	1427	(T+S)*F	F/999	(T+S)/200	12095765
3311	17	3591	0.318	1142	(T+S)*F	F/999	(T+S)/200	9433988
3312	17	2593	0.316	819	(T+S)*F	F/999	(T+S)/200	6810116
sum		18818		5462			(T+S)/200	48769303
3313	18	4519	0.331	1496	(T+S)*F	F/999	(T+S)/200	11047925
3314	18	3745	0.325	1217	(T+S)*F	F/999	(T+S)/200	9668541
3317	18	3243	0.330	1070	(T+S)*F	F/999	(T+S)/200	8301626
3318	18	4119	0.340	1400	(T+S)*F	F/999	(T+S)/200	10506790
3319	18	3800	0.331	1258	(T+S)*F	F/999	(T+S)/200	9779000
3320	18	3438	0.371	1276	(T+S)*F	F/999	(T+S)/200	8247984
3321	18	3885	0.323	1255	(T+S)*F	F/999	(T+S)/200	10045004
sum		26750		8972				67596870

Run	Tape	meas. time	trig_in/ trig_out	effect. time	Trigger $T1$	Trigger $T2$	Trigger $T3$	Events
3323	19	4351	0.316	1375	(T+S)*F	F/999	(T+S)/200	11356586
3324	19	5227	0.327	1709	(T+S)*F	F/999	(T+S)/200	13431970
3326	19	5189	0.515	2672	(T[K]+S)*F	F/999	(T+S)/200	10027102
3327	19	5081	0.505	2566	(T[K]+S)*F	F/999	(T+S)/200	10011623
3328	19	5070	0.499	2530	(T[K]+S)*F	F/999	(T+S)/200	10065116
3329	19	5296	0.498	2637	(T[K]+S)*F	F/999	(T+S)/200	10161949
3330	19	2746	0.472	1296	(T[K]+S)*F	F/999	(T+S)/200	5717686
sum		32960		14786			(T+S)/200	70772032
3331	20	4926	0.463	2281	(T[K]+S)*F	F/999	(T+S)/200	10385353
3332	20	5362	0.470	2520	(T[K]+S)*F	F/999	(T+S)/200	11209387
3333	20	5065	0.461	2335	(T[K]+S)*F	F/999	(T+S)/200	10756643
3334	20	5049	0.468	2363	(T[K]+S)*F	F/999	(T+S)/200	10565169
3335	20	4467	0.291	1300	(T+S)*F	F/999	(T+S)/200	12075704
3336	20	3030	0.296	897	(T+S)*F	F/999	(T+S)/200	8166763
3337	20	3472	0.485	1684	(T[K]+S)*F	F/999	(T+S)/200	6647417
sum		31370		13379				69806436
3339	21	6117	0.542	3316	(T[K]+S/3)*F	F/999		11190828
3340	21	6090	0.546	3325	(T[K]+S/3)*F	F/999		11029722
3341	21	5835	0.548	3198	(T[K]+S/3)*F	F/999		10532410
3342	21	5478	0.538	2947	(T[K]+S/3)*F	F/999		10023792
3343	21	5768	0.526	3034	(T[K]+S/3)*F	F/999		10810400
sum		29288		15819				53587152
3344	22	5868	0.523	3069	(T[K]+S/3)*F	F/999		11113485
3345	22	5498	0.527	2898	(T[K]+S/3)*F	F/999		10382343
3346	22	3906	0.527	2058	(T[K]+S/3)*F	F/999		7364292
3347	22	5947	0.259	1540	(T+S/3)*F	F/999	(T+S)/200	16850507
3348	22	7709	0.524	4039	(T[K]+S/3)*F	F/999		14670822
sum		28928		13604				60381449
3349	23	468	0.530	248	(T[K]+S/3)*F	F/999		870670
3350	23	8032	0.528	4241	(T[K]+S/3)*F	F/999		15133667
3351	23	1537	0.532	817	(T[K]+S/3)*F	F/999		2879791
3352	23	8152	0.537	4378	(T[K]+S/3)*F	F/999		15074107
sum		18189		9684				33958235
3358	24	5606	0.546	3061	(T[K]+S/3)*F	F/999		10192222
3359	24	5229	0.553	2892	(T[K]+S/3)*F	F/999		9372510
3360	24	5794	0.290	1680	(T+S)*F	F/999		12612040

Run	Tape	meas. time	trig_in/ trig_out	effect. time	Trigger $T1$	Trigger $T2$	Trigger $T3$	Events
sum		16629		7633				32176772
3365	25	5170	0.492	2543	(T[K]+S/3)*F	F/999		10437770
3366	25	5340	0.476	2542	(T[K]+S/3)*F	F/999		10333286
3367	25	5413	0.465	2517	(T[K]+S/3)*F	F/999		11386991
3368	25	4733	0.480	2272	(T[K]+S/3)*F	F/999		9719868
3369	25	3838	0.487	1869	(T[K]+S/3)*F	F/999		7785434
sum		24493		11743				49663349
total sum		300022		122619				684760272

Table A.1: List of the runs used in this analysis. The trigger notation is the following: T means telescopes, S sidewall and F forward. With the setting (T[K]+S/3)\*F a trigger signal was generated when either a particle hit was registered in one of the telescopes OR one of the sidewall counters AND a hit in one of the forward counters (layer 1 OR layer 2). In the case of a hit in the telescopes, the particle must have the TOF of a kaon (T[K]), while the sidewall count rate was prescaled with a factor of 1/3 with the above setting.

## A.2 Description of Angular Distributions

The most general form of the reaction amplitude for the  $Sp$  final state may be written as (see Ref. [Cer02])

$$\begin{aligned} \mathcal{M}_{Sp} = & a_{Sp} (\mathbf{p} \cdot \mathbf{S}) (\mathbf{k} \cdot \boldsymbol{\epsilon}^*) + b_{Sp} (\mathbf{p} \cdot \mathbf{k}) (\mathbf{S} \cdot \boldsymbol{\epsilon}^*) + \\ & c_{Sp} (\mathbf{k} \cdot \mathbf{S}) (\mathbf{p} \cdot \boldsymbol{\epsilon}^*) + d_{Sp} (\mathbf{p} \cdot \mathbf{S}) (\mathbf{p} \cdot \boldsymbol{\epsilon}^*) (\mathbf{k} \cdot \mathbf{p}) \end{aligned} \quad (\text{A.1})$$

and for the  $Ps$  final state as

$$\begin{aligned} \mathcal{M}_{Ps} = & a_{Ps} (\mathbf{p} \cdot \mathbf{S}) (\mathbf{q} \cdot \boldsymbol{\epsilon}^*) + b_{Ps} (\mathbf{p} \cdot \mathbf{q}) (\mathbf{S} \cdot \boldsymbol{\epsilon}^*) + \\ & c_{Ps} (\mathbf{q} \cdot \mathbf{S}) (\mathbf{p} \cdot \boldsymbol{\epsilon}^*) + d_{Ps} (\mathbf{p} \cdot \mathbf{S}) (\mathbf{p} \cdot \boldsymbol{\epsilon}^*) (\mathbf{q} \cdot \mathbf{p}). \end{aligned} \quad (\text{A.2})$$

$\mathbf{p}$ ,  $\mathbf{k}$  and  $\mathbf{q}$  are the cms-momenta of the proton beam, the deuteron and the relative momentum vector of the two kaons.  $\mathbf{S}$  is the spin of the initial proton pair,  $\boldsymbol{\epsilon}$  the polarization vector of the outgoing deuteron. The coefficients a, b, c and d are independent complex scalar amplitudes, only weakly depending on the total CM-energy.

The squared matrix element  $\overline{|\mathcal{M}|^2}$ , averaged over the initial spins and summed over the final spins has been calculated ([Han02]):

$$\begin{aligned} \overline{|\mathcal{M}|^2} = & C_0 + C_{pk2} \frac{(\mathbf{p} \cdot \mathbf{k})^2}{p^2 k^2} + C_{pq2} \frac{(\mathbf{p} \cdot \mathbf{q})^2}{p^2 q^2} + \\ & C_{qk} \frac{(\mathbf{k} \cdot \mathbf{q})}{kq} + C_{pkpq} \frac{(\mathbf{p} \cdot \mathbf{k})(\mathbf{p} \cdot \mathbf{q})}{p^2 kq} \end{aligned} \quad (\text{A.3})$$

with the constants

$$\begin{aligned} C_0 &= \frac{1}{2} p^2 k^2 (|a_{Sp}|^2 + |c_{Sp}|^2) + p^2 q^2 (|a_{Ps}|^2 + |c_{Ps}|^2), \\ C_{pk2} &= p^2 k^2 [ |b_{Sp}|^2 + \frac{1}{2} |b_{Sp} + p^2 d_{Sp}|^2 + \\ & \quad \text{Re} (a_{Sp}^* c_{Sp} + (a_{Sp} + c_{Sp})^* (b_{Sp} + p^2 d_{Sp})) ], \\ C_{pq2} &= p^2 q^2 [ |b_{Ps}|^2 + \frac{1}{2} |b_{Ps} + p^2 d_{Ps}|^2 + \\ & \quad \text{Re} (a_{Ps}^* c_{Ps} + (a_{Ps} + c_{Ps})^* (b_{Ps} + p^2 d_{Ps})) ], \\ C_{qk} &= kq p^2 \text{Re} (a_{Ps} a_{Sp}^* + c_{Ps} c_{Sp}^*), \\ C_{pkpq} &= p^2 kq \text{Re} ((a_{Ps} + b_{Ps} + c_{Ps} + p^2 d_{Ps})^* (a_{Sp} + b_{Sp} + c_{Sp} + p^2 d_{Sp}) + \\ & \quad 2b_{Ps}^* b_{Sp}). \end{aligned} \quad (\text{A.4})$$

With the definition of the three angles  $x = \frac{1}{pk}(\mathbf{p} \cdot \mathbf{k})$ ,  $y = \frac{1}{pq}(\mathbf{q} \cdot \mathbf{p})$  and  $z = \frac{1}{qk}(\mathbf{q} \cdot \mathbf{k})$  Eq. A.3 can be re-expressed. Integration over the azimuthal angle of the deuteron (unpolarized measurement) and over two of the above angles leads to the following dependences:

$$\begin{aligned} \frac{d\sigma}{dx} &\propto C_0 + \frac{1}{3}C_{pq2} + x^2C_{pk2} \\ \frac{d\sigma}{dy} &\propto C_0 + \frac{1}{3}C_{pk2} + y^2C_{pq2} \\ \frac{d\sigma}{dz} &\propto C_0 + \frac{1}{3}(C_{pq2} + C_{pk2}) + z(C_{qk} + \frac{1}{3}C_{pkpq}) \end{aligned} \quad (\text{A.5})$$

By fitting the corresponding experimental angular distributions four of the five parameters can be extracted.

If there are only S-waves in the  $K\bar{K}$  system involved ( $Sp$  configuration) all terms in Eq. A.4 which are due to the  $Ps$  configuration are zero. Thus,  $C_{pq2}$ ,  $C_{qk}$  and  $C_{pkqp}$  are also zero and  $\frac{d\sigma}{dy}$  and  $\frac{d\sigma}{dz}$  are proportional to a constant.

Analogous arguments can be used for the  $Ps$  configuration where  $\frac{d\sigma}{dx}$  and  $\frac{d\sigma}{dz}$  would be proportional to a constant. In the reaction  $pp \rightarrow da_0^+ \rightarrow dK^+\bar{K}^0$  only the configuration  $Sp$  is possible if higher partial waves are suppressed.

# Bibliography

- [Abe98] A. Abele *et al.*, Phys. Rev. **D 57** (1998) 3860
- [Abo70] M. A. Abolins *et al.*, Phys. Rev. Lett. **25** (1970) 469
- [Alb97] D. Albers *et al.*, Phys. Rev. Lett. **78** (1997) 1652
- [Ams92] C. Amsler *et al.*, Phys. Lett. **B 291** (1992) 347
- [Ams94a] C. Amsler *et al.*, Phys. Lett. **B 327** (1994) 425
- [Ams94b] C. Amsler *et al.*, Phys. Lett. **B 333** (1994) 277
- [Ani00] V. V. Anisovich *et al.*, Phys. Lett. **B 480** (2000) 19
- [Ant86] D. Antreasyan *et al.*, Phys. Rev. **D 33** (1986) 1847
- [Arc02] P. Archard *et al.*, Phys. Lett. **B 526** (2002) 269
- [Ast67] A. Astier *et al.*, Phys. Lett. **25 B** (1967) 294
- [Atk84] M. Atkinson *et al.*, Phys. Lett. **138 B** (1984) 459
- [Bal01] F. Balestra *et al.*, Phys. Rev. **C 63** (2001) 024004
- [Bar97a] D. Barberis *et al.*, Phys. Lett. **B 413** (1997) 217
- [Bar97b] D. Barberis *et al.*, Phys. Lett. **B 413** (1997) 225
- [Bar98] D. Barberis *et al.*, Phys. Lett. **B 440** (1998) 225
- [Bar00] D. Barberis *et al.*, Phys. Lett. **B 488** (2000) 225
- [Bar01] S. Barsov *et al.*, NIM **A 462** (2001) 364
- [Bel99] F. Bellemann *et al.*, Phys. Rev. **C 60** (1999) 061002 (R)
- [Ber98] A. Bertin *et al.*, Phys. Lett. **B 434** (1998) 180

- [Bet99] M. Betigeri *et al.*, Nucl. Instr. and Meth. **A 421** (1999) 447
- [Bev02] E. van Beveren and G. Rupp, arXiv:hep-ph/0201006
- [Boh00] A. Bohm *et al.*, Nucl. Instr. and Meth. **A 443** (2000) 238
- [Bou98] A. Boukharov *et al.*, Int. Conf. CRYOGENICS98, Prague, Czech Republic, May 1998, Ann. Report 1997, IKP, FZ-Jülich, Report Jül3505, p. 63
- [Bra96] S. Brauksiepe *et al.*, Nucl. Instr. and Meth. **A 376** (1996) 397
- [Bra02] E. Bratkovskaya *et al.*, J. Phys. **G 28** (2002) 2423
- [Büs01] M. Büscher, COSY proposal #97, 2001; available via [www.fz-juelich.de/ikp/anke/](http://www.fz-juelich.de/ikp/anke/)
- [Büs02a] M. Büscher *et al.*, Nucl. Instr. Meth. **A 481** (2002) 378
- [Büs02b] M. Büscher *et al.*, Proc. Workshop on the Future Physics Program at COSY (CSS 2002), Jülich, Germany, Sept. 2002, in print School (2002)
- [Cel00] L. S. Celenza *et al.*, Phys. Rev. **C 61** (2000) 035201
- [Cer97] V. Chernyshev, COSY proposal #55, 1997;  
M. Büscher, beamtime request for COSY proposal #55, 2000;  
M. Büscher, beamtime request for COSY proposal #55, 2001;  
available via [www.fz-juelich.de/ikp/anke/](http://www.fz-juelich.de/ikp/anke/)
- [Cer02] V. Chernyshev *et al.*, nucl-th/0110069 (2002)
- [Cla01] K. N. Clausen, Proc. 15th Meet. of the Int. Collab. on Advanced Neutron Sources, ICANS-XV (2001), 27
- [Clo92] F. E. Close and N. A. Tornqvist, arXiv:hep-ph/0204205
- [DeB80] L. de Billy *et al.*, Nucl. Phys. **B 176** (1980) 1
- [Def72] C. Defoix *et al.*, Nucl. Phys. **B 44** (1972) 125
- [Dym01] S. Dymov, Annual Report 2001, IKP, FZ Jülich; available via [www.kfa-juelich.de/ikp/publications/AR2001](http://www.kfa-juelich.de/ikp/publications/AR2001)
- [Enk99] M. Enke *et al.*, Nucl. Phys. **A 657** (1999) 317
- [Eva81] C. Evangelista *et al.*, Nucl. Phys. **B 178** (1981) 197



- [Fed01] P. Fedorets, Annual Report 2001, IKP, FZ Jülich; available via [www.kfa-juelich.de/ikp/publications/AR2001](http://www.kfa-juelich.de/ikp/publications/AR2001)
- [Fed02] P. Fedorets, PhD thesis, in progress
- [Fla76] S.M. Flatté, Phys. Lett. **63 B** (1976) 225
- [Gra77] H. Grassler *et al.*, Nucl. Phys. **B 121** (1977) 189
- [Gri00] V. Grishina *et al.*, Eur. Phys. J. **A 9** (2000) 277
- [Gri02] V. Grishina, Proc. 3<sup>rd</sup> ANKE Workshop, Swierk, Poland, May 2002, Berichte des Forschungszentrums Jülich **4000**
- [Gur79] A. Gurtu *et al.*, Nucl. Phys. **B 151** (1979) 181
- [Han02] C. Hanhart, “Private Communication”, 2002
- [Har01] M. Hartmann *et al.*, COSY Proposal #104, October 2001; available via [www.fz-juelich.de/ikp/anke](http://www.fz-juelich.de/ikp/anke)
- [Hej02] V. Hejny *et al.*, Nucl. Intr. Meth. **A 486** (2002) 126
- [Jun00] H. Junghans, Dissertation, Universität zu Köln (2000)
- [Kom02] V. Komarov *et al.*, arXiv:nucl-ex/0210017 (2002)
- [Leh00] I. Lehmann, Diplomarbeit, Universität zu Köln (2000)
- [Loh90] D. Lohse *et al.*, Nucl. Phys. **A 516** (1990) 513
- [Mai97] R. Maier, Nucl. Intr. and Meth. **A 390** (1997) 1
- [Mik02] M. Mikirtychians *et al.*, Proc. 9th Int. Conf. on Pol. Sources and Targets, Nashville, Indiana, USA, October 2001, Eds. V.P.Derenchuk, B.v.Przewoski, World Scientific
- [Nar01] S. Narison, Nucl. Phys. Proc. Suppl. **96** (2001) 244
- [Oes90] T. Oest *et al.*, Zeit. f. Phys. **C 47** (1990) 343
- [Oll00] J. A. Oller *et al.*, Prog. Part. Nucl. Phys. **45** (2000) 157
- [Ose01] E. Oset *et al.*, Eur. Phys. J. **A 12** (2001) 435
- [PDG02] K. Hagiwara *et al.*, Phys. Rev. **D 66** (2002) 010001
- [PDG69] Particle Data Group, Rev. Mod. Phys. **Vol. 41** (1969) No.1, 109

- 
- [PDG71] Particle Data Group, Rev. Mod. Phys. **Vol. 43** (1971) No.2, S1
- [PDG73] Particle Data Group, Rev. Mod. Phys. **Vol. 45** (1973) No.2, S1
- [PDG80] Particle Data Group, Rev. Mod. Phys. **Vol. 52** (1980) No. 2, Part II (1980)
- [PDG86] Particle Data Group, Phys. Lett. **170 B** (1986) 1
- [PIS99] The PISA Collaboration, Annual Report 1999, IKP, FZ-Jlich, Report JI-3744, p. 175
- [Que01] C. Quentmeier *et al.*, Phys. Lett. **B 515** (2001) 276
- [Ric00] R. Ricken *et al.*, Eur. Phys. J. **A 9** (2000) 221
- [San97] R. Santo *et al.*, Nucl. Instr. Meth. **A 386** (1997) 228, A. Khoukaz *et al.*, Eur. Phys. J. **D 5** (1999) 275
- [Tei99] S. Teige *et al.*, Phys. Rev. **D 59** (1999) 012001
- [Tie01] H. Tietze-Jaensch *et al.*, Proc. 15th Meet. of the Int. Collab. on Advanced Neutron Sources, ICANS-XV (2001), 829
- [Vij02] J. Vijande *et al.*, arXiv:hep-ph/0206263
- [Vol91] A. D. Volkov *et al.*, Nucl. Instr. Meth. **A 306** (1991) 278
- [Wei83] J. D. Weinstein and N. Isgur, Phys. Rev. **D 27** (1983) 588
- [Zyc02] I. Zychor, Acta Physica Polonica **B 33** (2002) 521

# Acknowledgements

Finally, I would like to thank all those people from the institute and the ANKE collaboration who contributed to the development of this work.

In particular, I wish to thank Prof. Dr. H. Ströher for the interesting PhD topic and the possibility to work in his team in the Research Centre Jülich.

Many thanks to Prof. Dr. H. Paetz gen. Schieck and to Prof. Dr. C. Kiefer for acting as the co-referee and the chairman of the exam, respectively.

I wish to express my gratitude to Dr. Markus Büscher for listening to all my questions (I have to admit that he hardly had a chance to escape) and spending a lot of time on answering them.

I am much obliged to Dr. Vladimir Koptev who taught me how to handle this monster called sorter and how to interpret its throw-offs and who took a lot of time to explain the data analysis at ANKE.

Many thanks to Dr. Misha Nekipelov who helped me a lot during the beamtimes and with preparing a sorter which allowed me to analyse the data.

I am grateful to Dr. Ralf Schleichert for all the advice and his talent to motivate a frustrated PhD student (unavoidable from time to time...).

Thanks a lot to Dr. Volker Hejny and Dr. Michael Hartmann for the help with this pain in the neck named computer and the helpful advice in handling data.

Many thanks to Inti Lehmann, Ola Wronska, Sergej Dymov, Pawel Fedorets and all other (PhD) students for helping with the different questions and problems which pop up during three years of PhD.

Thanks a lot to Dr. Christoph Hanhart for the patience to teach me “some theory“. Some things I can even remember...

Many thanks to Dr. Jim Ritman for taking his time to give a lot of advice concerning the acceptance correction of the data (which almost drove me mad...).

I am obliged to Prof. Dr. Colin Wilkin who was unlucky with being in Jülich as the only native English speaker shortly before I had to submit my thesis and who consent to proof-read it (not that he had an alternative...).

Last but not least I am grateful to my boyfriend Velten Lichtenberger (who even moved to Tetz with me!) for the time outside of work and to my family for “emotional and moral assistance“.



# Erklärung

Ich versichere, dass ich die von mir vorgelegte Dissertation selbstständig angefertigt, die benutzten Quellen und Hilfsmittel vollständig angegeben und die Stellen der Arbeit - einschließlich Tabellen, Karten und Abbildungen - die anderen Werken im Wortlaut oder dem Sinn nach entnommen sind, in jedem Einzelfall als Entlehnung kenntlich gemacht habe; dass diese Dissertation noch keiner anderen Fakultät oder Universität zur Prüfung vorgelegen hat; dass sie - abgesehen von unten angegebenen Teilpublikationen - noch nicht veröffentlicht worden ist sowie, dass ich eine solche Veröffentlichung vor Abschluss des Promotionsverfahrens nicht vornehmen werde. Die Bestimmungen dieser Promotionsordnung sind mir bekannt. Die von mir vorgelegte Dissertation ist von Herrn Prof. Dr. H. Ströher betreut worden.

## Publikationen

- „ $a_0^+(980)$ -resonance production in  $pp \rightarrow dK^+ \bar{K}^0$  reactions close to threshold“, V. Kleber *et al.*, eingereicht bei Physical Review Letters
- International Conference on Quark Nuclear Physics, June 2002, Jülich, Germany (QNP2002),  
im Druck
- 5<sup>th</sup> International Conference on Nuclear Physics at Storage Rings, June 2002, Uppsala, Sweden (STORI02),  
im Druck
- International School of Nuclear Physics, 24<sup>th</sup> Course, September 2002, Erice, Sicily, Italy,  
V. Kleber *et al.*, Progress in Particle and Nuclear Physics 50 (2003), 557-559